

Seismic performance assessment of monopile-supported offshore wind turbines using unscaled natural earthquake records

Raffaele De Risi^{a,*}, Subhamoy Bhattacharya^b, Katsuichiro Goda^a

^a Department of Civil Engineering, Queen's Building, University Walk, University of Bristol, B8 1TR Bristol, UK

^b Department of Civil and Environmental Engineering, University of Surrey, GU2 7XH Guildford, UK

ARTICLE INFO

Keywords:

Wind turbines
Seismic performance
Crustal earthquakes
Inslab earthquakes
Interface earthquakes
Soil-structure interaction

ABSTRACT

The number of offshore wind turbine farms in seismic regions has been increasing globally. The seismic performance of steel monopile-supported wind turbines, which are the most popular among viable structural systems, has not been investigated thoroughly and more studies are needed to understand the potential vulnerability of these structures during extreme seismic events and to develop more reliable design and assessment procedures. This study investigates the structural performance assessment of a typical offshore wind turbine subjected to strong ground motions. Finite element models of an offshore wind turbine are developed and subjected to unscaled natural seismic records. For the first time, the sensitivity to earthquake types (i.e. crustal, inslab, and interface) and the influence of soil deformability and modeling details are investigated through cloud-based seismic fragility analysis. It is observed that monopile-supported offshore wind turbines are particularly vulnerable to extreme crustal and interface earthquakes, and the vulnerability increases when the structure is supported by soft soils. Moreover, a refined structural modeling is generally necessary to avoid overestimation of the seismic capacity of offshore wind turbines.

1. Introduction

Wind energy production from offshore wind farms is a reality nowadays around the world. Fig. 1 shows main countries that are developing and investing in offshore wind power according to the Global Wind Energy Council [1]. The same figure shows a global seismic hazard map in terms of peak ground acceleration (PGA) with probability of exceedance of 10% in 50 years [2]. Several countries are in high seismic regions, including the USA, China, India, and South East Asia, and are adjacent to subduction zones (blue lines in Fig. 1), where magnitude M9-class megathrust earthquakes can occur. This highlights that earthquake risk for newly built offshore wind farms can be potentially high and that reliable design and assessment methods for these structures against intense ground excitations need to be developed. In fact, current international standards and national codes (e.g., GL [3], DNV [4], IEC [5]) suggest considering seismic actions but without explaining in detail how to evaluate the seismic performance (e.g. suitable analysis methods). The lack of basic research that underpins codes' requirements may be related to the limited number of wind turbines that were actually damaged during major earthquakes [6,7]. Moreover, structural damage to wind turbines was mainly reported for onshore wind turbines, thus contributing to common misperception that seismic

loading is not critical for offshore wind turbine structures [8]. On the other hand, the global development of such structures in active seismic regions makes imperative to understand to which extent structural demand on offshore wind turbines is increased by earthquake loads, and whether numerical results may be affected by modeling details or by the implementation of the soil-structure interaction (SSI) that has been recognized playing a very important role on the structural performance [9,10].

Literature on seismic behavior of offshore wind turbines is not as extensive as for the case of onshore wind turbines [11,12]. Hacıfendioglu [13] investigated a 3-MegaWatt (MW) offshore monopile-supported wind turbine in a comprehensive manner, developing a full three-dimensional (3D) model considering the ensemble structure, soil, and water. In that study, a single stochastic earthquake was applied to the structure considering the rotor in a parked state, and the effects of seawater level, soil conditions, and the presence of floating ice sheets were investigated. Mardfekri and Gardoni [14], given high sophistication of the required numerical models and high computational costs, attempted to substitute a refined 3D model with a probabilistic surrogate model represented by a simpler model and model correction terms for developing seismic fragility curves. Kim et al. [15] analyzed the seismic response of a 5-MW offshore monopile-supported wind turbine

* Corresponding author.

E-mail addresses: raffaele.derisi@bristol.ac.uk (R. De Risi), s.bhattacharya@surrey.ac.uk (S. Bhattacharya), katsu.goda@bristol.ac.uk (K. Goda).

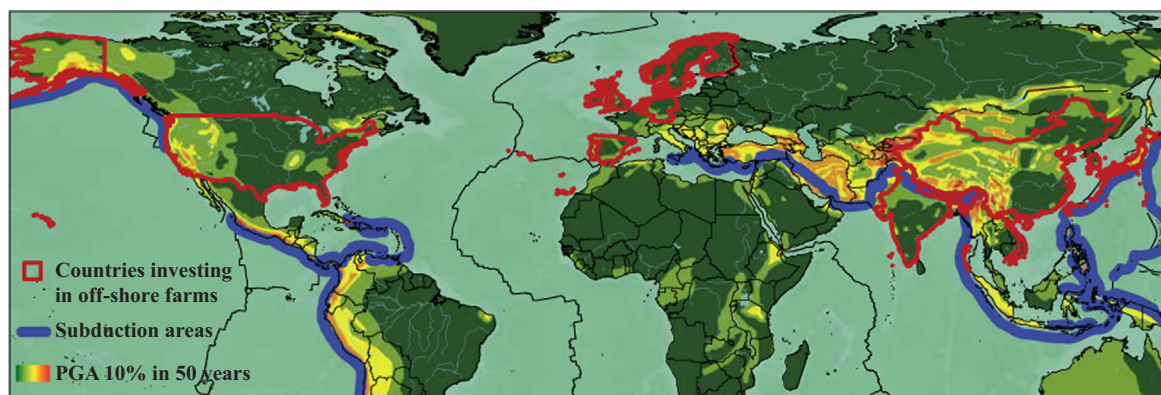


Fig. 1. Map of countries investing in offshore wind farms (red boundaries), subduction trenches (blue lines), and global seismic hazard map. (For interpretation of the references to color in this figure legend, the reader is referred to the web version of this article.)

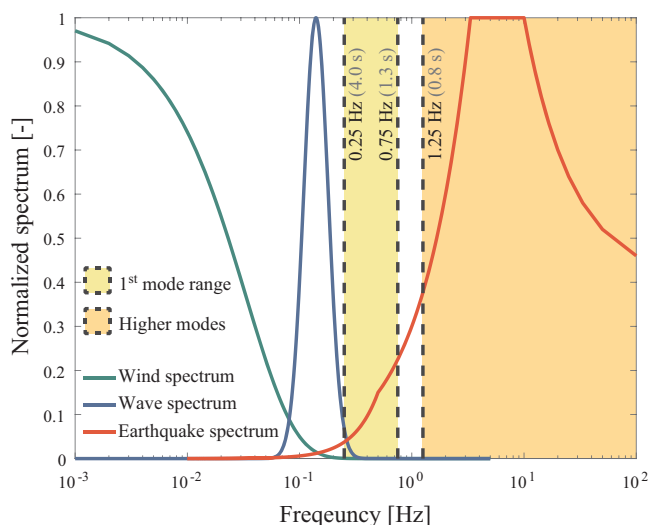


Fig. 2. Typical normalized spectra of actions due to wind, sea waves, and earthquake ground motions. The yellow and orange bands represent the ranges of vibration periods for conventional wind turbines corresponding to main and higher modes, respectively. (For interpretation of the references to color in this figure legend, the reader is referred to the web version of this article.)

to obtain seismic fragility curves. They used a simplified model with lumped masses for the main support structure and modeled the soil with nonlinear springs; two natural and several artificial input ground motions were adopted in the analyses. Attention is paid to how to apply the seismic loading to the structure at the foundation considering either the case of applying different motions at each support or the case of applying the same motion to all supports. They observed that the variation of seismic motion in layered soils plays an important role in the fragility assessment. Kim et al. [16] performed for the first time a reliability analysis of a jacket-type offshore wind turbine structure adopting a first order reliability method performing static and dynamic analyses using a large number of artificial earthquakes. They concluded that the probability of failure is mainly influenced by the seismic factor and it is essential to perform dynamic analyses. Recently, Zheng et al. [17] performed shaking table tests of a scaled model of a 5-MW offshore monopile-supported wind turbine concluding that peak accelerations excited by earthquake and moderate sea conditions (that are currently considered in the design) were comparable. Moreover, Alati et al. [18] were the first in studying offshore wind turbines with a dedicated software package using 25 natural records to derive information on the structural demand by performing coupled analyses with all other dynamic phenomena acting upon the structure. They focused upon tripod and jacket support systems, instead of monopile support, which are

more suitable for transitional water depth (30–60 m); they did not derive any fragility curves. At the same time, Chen et al. [19] proposed a design procedure to optimize hybrid jacket-hybrid off-shore wind turbine structures. Finally, more features are implemented in the FAST code [20], a comprehensive aeroelastic simulator developed by the National Renewable Energy Laboratory (NREL, <https://nwtc.nrel.gov/FAST>), to improve the seismic capabilities of the tool and to allow the implementation of the soil structure interaction in offshore conditions [21].

All previous investigations focused on specific details but are not thorough from a seismic point of view, especially for monopile-supported offshore wind turbines. The number of records used in the analyses is small. Moreover, the adoption of specialized not open-source software tools did not allow to have the full control of the modeling. It is important to highlight that wind turbines should be assessed by considering more extreme conditions, noting that existing wind turbines did not experience the most critical shaking as their spatial distributions are sparse.

This paper presents new findings and insight regarding the seismic performance of steel monopile-supported offshore wind turbines, which is the most common system around the world since it has been proved to be economical at shallow water depth [22]. Moreover, tubular steel towers are very popular in the industry because of their esthetically pleasing look, good dynamic behavior, fatigue resistance, and identical bending stiffness in all directions [19]. Monopile-supported offshore wind turbines are typically characterized by the first vibration periods in the range between 1.3 and 4 s, and higher-mode vibration periods lower than 0.8 s [23]. Fig. 2 shows normalized spectra for typical wind, sea wave, and ground shaking (the latter is a typical normalized Eurocode 8 response spectrum [24]); on the same figure, the ranges of periods for the first vibration modes and higher modes are also included. It is possible to observe that the first modes usually fall in the range of periods where the spectral content of earthquake ground motions decays but is still relatively high (depending on the characteristics of earthquake scenarios and local site conditions). Therefore, it is essential to understand which seismic events and soil conditions may excite such periods, and if higher modes play significant role in the seismic behavior.

The seismic performance of the wind turbine models is analyzed by performing nonlinear dynamic analysis (NDA). Two limit states, i.e. the serviceability (SLS) and the ultimate (ULS) limit states, are investigated by monitoring the deformation and the internal stresses, respectively. A large number of strong motions records that are obtained from different seismic environments are used as input time-histories in NDA. The investigation of different earthquake types on offshore wind turbine structures does not exist in literature and is performed for the first time. Specifically, five aspects of the seismic performance are investigated in this study. First, the influence of the earthquake record characteristics

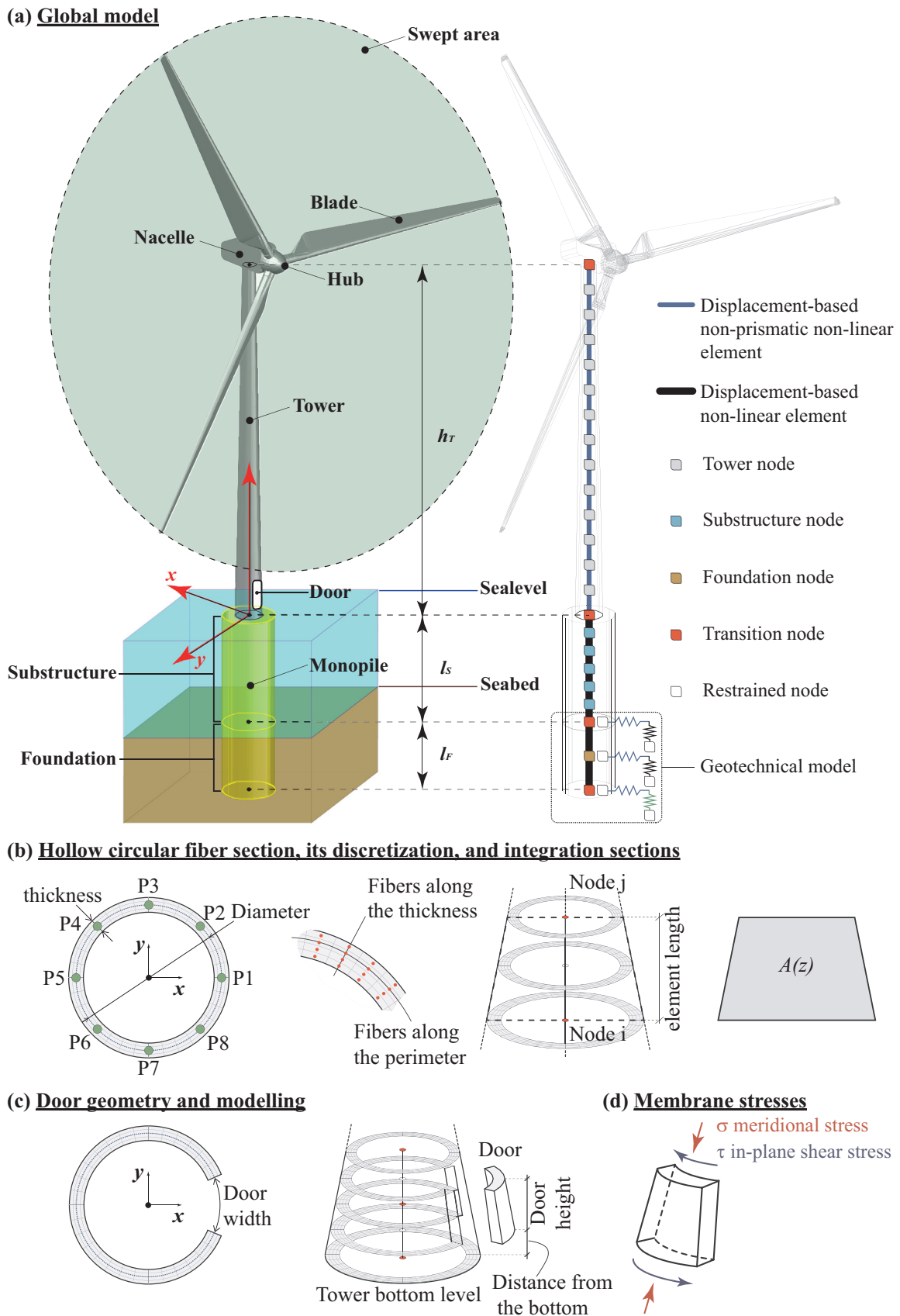


Fig. 3. (a) Components of the wind turbine, coordinate reference system, and schematic representation of the assembly model, (b) hollow circular fiber section, its discretization, and integration sections along the element, (c) geometric characteristics of the door and its modeling using C-shape sections, and (d) membrane stresses.

on the structural response is examined using unscaled ground motion records from crustal, inslab and interface earthquakes in NDA. Such investigations are necessary since many wind farms will be built in subduction areas, as shown in Fig. 1, where all three earthquake types can occur. Second, the influence of the SSI is investigated by considering three different modeling options: (i) a sophisticated nonlinear foundation model, (ii) a discrete spring system based on impedance functions, and (iii) fixed boundary conditions. Third, the effect of different frequency contents associated with records characterized by different shear wave velocity (V_{S30}) profiles is investigated using two sets of crustal ground motion records characterized by different V_{S30} values. Fourth, the influence of the door opening at the tower base is investigated. Such an access point is usually necessary to enter the structure and reach the nacelle by an internal ladder. To date, other weakness points have been studied, such as the transition piece between the substructure and the tower, generally realized by means of a grouted connection and a shear key [25,26]; on the contrary, the modeling of the opening has not been investigated thoroughly. Such a modeling detail is necessary since the opening creates a weak point within the structure due to the high concentration of stress [27]. Finally, a steel material that degrades in compression for the potential buckling is adopted to investigate the effects on the seismic performance of the offshore wind turbines.

2. Modeling, limit states, and analysis setup

2.1. Basic definitions and case study

Fig. 3a shows different parts of a typical monopile offshore wind turbine. The blades are connected to the hub. Blades and hub altogether are referred to as rotor. The circular area described by the rotor is called as swept area. The hub is connected to the generator that is placed inside the nacelle. The nacelle transfers the load on rotor to the support tower structure. The support structure of the wind turbine is composed by two elements: the tower and the monopile, which is composed by substructure and foundation. The tower is the part of the support structure which connects the sub-structure to the rotor-nacelle assembly. Generally, the tower is modeled as a truncated cone having the largest diameter at the base and the smallest at the top. The substructure is the part of the support structure that extends upward from the seabed and connects the foundation to the tower. The foundation is the part of the support structure that transfers the loads acting on the sub-structure into the seabed. At the base of the tower, an opening is generally placed, which is the entrance door allowing the access to the top part of the tower through an internal ladder. The reference coordinate system adopted within the numerical model is shown in red in Fig. 3a. Specifically, the x axis is along the central axis of the rotor (i.e. long direction of the nacelle), the y axis is orthogonal to the x-axis and belongs to the horizontal plane, and the z-axis is the vertical axis.

In this study, the Vestas V66 industrial offshore wind turbine, capable of generating 2-MW of power, is selected. The geometrical characteristics of the entire system are retrieved from Arany et al. [23], and are listed in Table 1. The considered steel material is S355 [28] having the yield strength (f_y) of 355 MPa and the modulus of elasticity (E) of 210 GPa.

2.2. Structural model

The structural model developed is an intermediate solution between a comprehensive 3D nonlinear model (e.g. nonlinear shells for the structure and brick elements for the soil) and a 3D simplified model (e.g. linear beam fixed at the seabed); such modeling allows obtaining results with a reasonable computational effort and at the same time with a good degree of reliability. The open-source structural software OpenSees [29] is adopted to model the structure and perform the seismic response analyses. Figs. 3–6 show an overview of the modeling

Table 1
Input parameters for the selected wind turbine.

Parameter	Symbol	
Mass of the rotor-nacelle assembly	m	80 ton
Tower height	h_T	54.5 m
Tower bottom diameter	d_B	4.25 m
Tower top diameter	d_T	2.75 m
Average tower wall thickness	t_T	34 mm
Platform height above the mudline (i.e. substructure length)	l_S	16.5 m
Pile embedded length (i.e. foundation length)	l_F	15.0 m
Monopile diameter	d_M	3.5 m
Monopile wall thickness	t_M	50 mm

assumptions explained in detail in the following. It is emphasized that a co-rotational formulation is adopted for the coordinate-transformation object to analyze the structure in the large-displacement – small strain framework. Such an option allows to deal with potential global nonlinear instability of the structural system.

It is important to underline that reasonable simplifications in structural modeling are made; such assumptions can be considered robust enough especially given the comparative nature of the presented results. In fact, similarities and differences are assessed with the same basic hypotheses in relative rather than absolute terms.

2.2.1. Tower

The tower is modeled with nonlinear displacement-based elements (blue lines in Fig. 3a). Such modeling allows the definition of non-prismatic elements, i.e. elements having different sections along the axis (Fig. 3b). The adoption of displacement-based elements requires a refined discretization of the tower into many elements; in this study, a discretization of 0.5 m is adopted. Given the fine discretization, each structural element is composed of three integration points, two at both ends and one in the middle (Fig. 3b). The element section is modeled as a circular hollow fiber section with 1000 fibers along the perimeter and 4 fibers along the thickness (Fig. 3b). During the analysis, stress values of eight equally-spaced points (i.e. at interval of 45 degrees, depicted as green points in Fig. 3b) along the section perimeter are monitored. In this study, bolted connections between different tower segments are neglected in the modeling.

The presence of a door at the bottom of the tower will constitute a structural weakness in the tower. Fig. 3c shows a schematic representation of the door opening and its modeling in the structural system. Specifically, the implementation of the door is carried out by varying the section along the structural elements intersected by the door; “C” shape sections are used instead of the hollow circular sections.

2.2.2. Monopile

The monopile is modeled with cylindrical nonlinear displacement-based elements; as per the tower, circular fiber hollow sections are adopted. Also for the monopile a 0.5-m discretization and three integration points are used for each element. Points along the entire length of the monopile shown in Fig. 3b are monitored during the analysis. The part of the monopile belonging to the foundation requires more detailed modeling. In this study, three different modeling options are adopted: (a) the nonlinear Winkler beam (NWB, Fig. 4a), (b) the discrete representation of the foundation through impedance functions (IF, Fig. 4b), and (c) the fixed restraint (FR, Fig. 4c).

For the nonlinear Winkler foundation, a procedure detailed in McGann et al. [30,31] is adopted (Fig. 4a). Specifically, nonlinear springs are adopted to model the vertical and horizontal mechanical behavior of the surrounding soil. The soil springs are generated using zero-length elements characterized by independent uniaxial material along the horizontal and vertical directions. The modeling of the soil requires the inclusion of two additional nodes for each node of the pile:

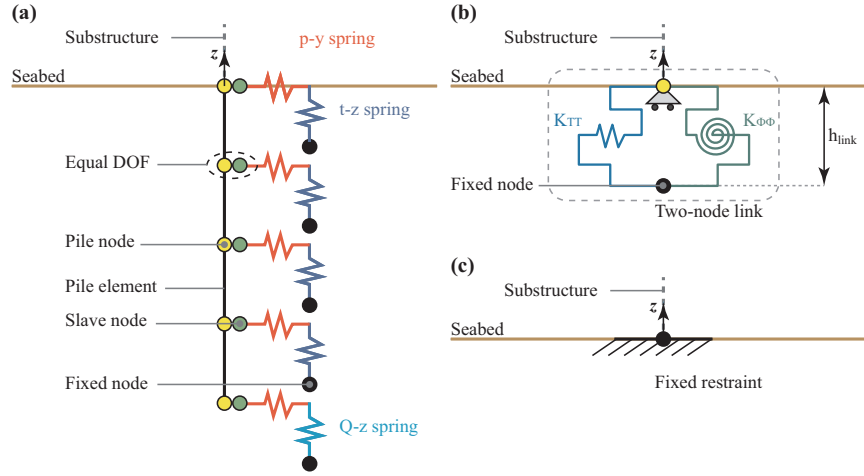


Fig. 4. Different foundation models: (a) nonlinear Winkler beam, (b) impedance function-based model, and (c) fixed restraint.

a fixed node that is fully constrained, and a slave node that is constrained for rotation but is not constrained for translation. The zero-length element is placed between the two nodes. The constitutive behavior of the two elements is characterized such that the springs oriented in the horizontal directions (i.e. x and y) represent p-y springs, and the vertically-oriented springs represent t-z and Q-z behavior for the pile shaft and tip, respectively [32]. The *PySimple1* material objects are used for the horizontal directions, while the *TzSimple1* and the *QzSimple1*, material objects for the shaft and the tip, respectively, are used for the vertical direction. Such schematization can be adopted also in the case of liquefiable soils adopting modified p-y springs [33]. The main geotechnical properties are the soil unit weight, assumed equal to 18.5 kN/m³, the soil internal friction angle, assumed equal to 35° [34], and the soil shear modulus at pile tip, assumed equal to 250 MPa. For the *PySimple1* material, the API [35] suggestions are adopted for the ultimate load curves and for the coefficient of subgrade reaction with depth. For the *TzSimple1* material, the backbone curve proposed by Mosher [36] is adopted. Finally, for the *QzSimple1* material, the backbone curve proposed by Vijayvergiya [37] is adopted. Additional information on the modeling can be found in the OpenSees online manual,¹ where the adopted modeling approach and its accuracy/reliability have been verified against other available software packages.

It is important to emphasize that in general, nonlinear horizontal beams should be coupled in parallel with dashpots modeling the radiation damping [38,39]. In this study, this additional modeling detail is neglected since in stiff soil an additional dashpot can lead to unrealistic damping force in the dynamic analysis [40]. Moreover, radiation damping (a.k.a. geometric dissipation of waves from spreading) is negligible for frequency less than 1 Hz [21,34]. Finally, different damping values for each vibration mode cannot be applied with the Rayleigh damping scheme, presented later in Section 2.2.5.

As a simplified method for capturing the soil-structure interaction, the discrete representation of the soil-structure interaction through impedance functions [41] is considered. In this method, piles having aspect ratio similar to the examined case, located in parabolic-inhomogeneous soils, can be substituted by the following impedance functions:

$$K_{TT} = 5.33 \cdot \left(\frac{l_f}{d_f}\right)^{1.07} \cdot f(\nu_s) \cdot E_s \cdot r \quad (1)$$

$$K_{\phi\phi} = 13 \cdot \left(\frac{l_f}{d_f}\right)^3 \cdot f(\nu_s) \cdot E_s \cdot r^3 \quad (2)$$

$$K_{T\phi} = 7.2 \cdot \left(\frac{l_f}{d_f}\right)^2 \cdot f(\nu_s) \cdot E_s \cdot r^2 \quad (3)$$

where K_{TT} , $K_{\phi\phi}$ and $K_{T\phi}$ are the impedance functions for pure horizontal translation, pure rotation, and coupled translation-rotation, respectively. l_f , d_f and r are the pile length, diameter, and radius, respectively. E_s and ν_s are the initial Young's modulus and Poisson ratio of soil, respectively, which are assumed equal to 200 MPa and 0.25. Finally, $f(\nu_s)$ is a function of the Poisson ratio and is given by:

$$f(\nu_s) = \frac{1 + \nu_s}{1 + 0.75 \cdot \nu_s} \quad (4)$$

It is worth noting that for the NWB model, the hysteretic damping is automatically considered in the model. For the IF model adopted in this study, such a source of damping is neglected. The modeling of impedance in OpenSees is carried out through the adoption of two-node link elements (Fig. 4b). Such an element requires the definition of the transversal (K_{TT}) and rotational ($K_{\phi\phi}$) stiffness values. Moreover, if the two nodes are located at a given distance (h_{link}) the coupling between the two springs is defined; h_{link} represents the ratio between $K_{T\phi}$ and K_{TT} .

2.2.3. Material modeling

The elasto-plastic material *Steel02* is adopted in OpenSees, also known as Giuffrè-Menegotto-Pinto Model [42] to model both the tower and the monopile. A strain hardening (b) of 0.5% is considered. To investigate asymmetric behavior in compression, the original *Steel02* model is modified to account for the degrading behavior due to buckling defining a negative isotropic hardening (ih) of -5%, which is different from zero. Fig. 5 shows the hysteretic behavior of the adopted material models, neglecting (Fig. 5a) and considering (Fig. 5b) the degrading behavior in compression. The fatigue is also implemented by defining the *fatigue* material object in OpenSees; such a material uses a modified rain-flow cycle counting algorithm to accumulate damage in a material using Miner's rule based on Coffin-Manson log-log relationships describing low-cycle fatigue failure. The default values of the parameters were based on low-cycle fatigue tests of European steel sections [43]; more information about how material was calibrated can be found in Uriz [44].

2.2.4. Inertia characteristics

Masses are lumped at the structural joints; four cases need to be discussed: (a) tower joints, (b) substructure joints, (c) foundation joints, and (d) transition joints (see Fig. 3a for the definition of joint typologies). At the tower joints, only the structural mass is applied. For substructure and foundation joints tributary mass of water and soil, respectively, should be considered [16]. For substructure joints, aside from the structural mass,

¹ http://opensees.berkeley.edu/wiki/index.php/Laterally-Loaded_Pile_Foundation.

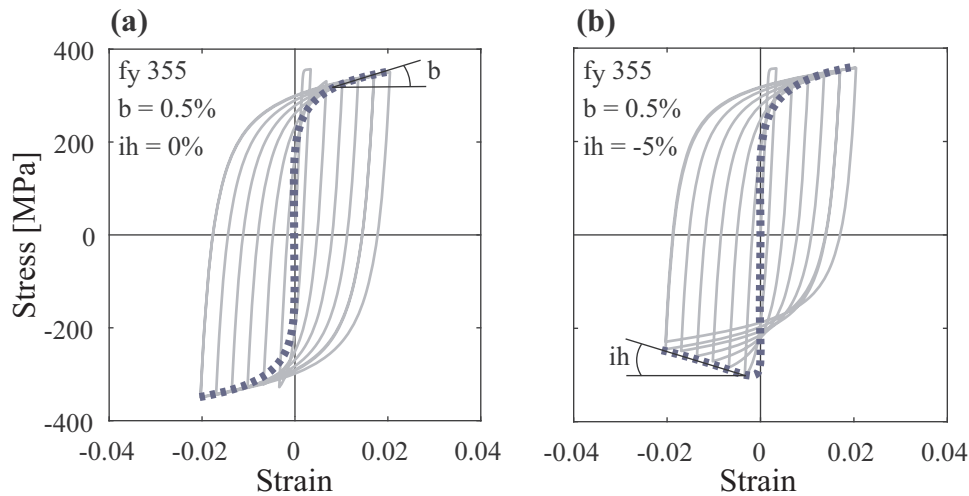


Fig. 5. (a) Non-degrading, and (b) degrading steel material.

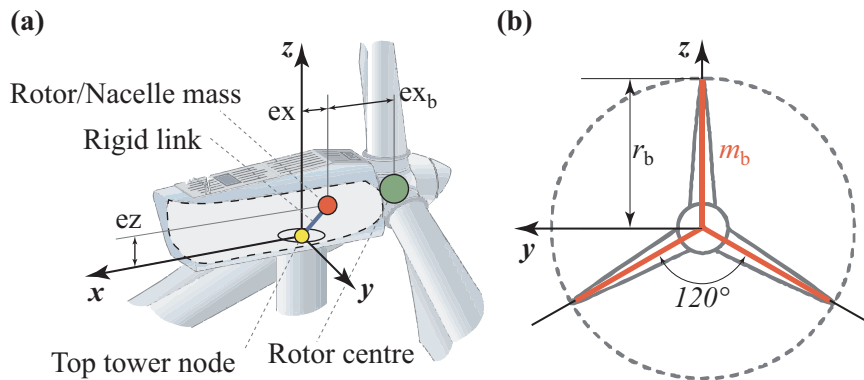


Fig. 6. (a) Inertia modeling of the rotor/nacelle assembly, and (b) schematic representation of the rotor.

additional tributary mass of water is considered. Specifically, the tributary mass is effective only for the horizontal translation components and it is calculated equal to 80% of a mass of a cylinder of water with diameter and length having the same dimension as the submerged part [45]. Finally, the mass of the foundation nodes is lumped at the discretized points. The mass is calculated as the sum of the structural part, the soil inside the cylinder, and a tributary mass of an additional cylinder of soil having the same dimension as the pile. Also in this case the additional tributary mass is considered for the horizontal components only. The transitional masses of the joints come from contributions of the structural part they connect.

A specific attention is dedicated in this study to the top joint. The definition of the translational and rotational masses of the top part of the wind turbine is important since it allows simplifying the complex modeling of the rotor/nacelle assembly, while keeping a realistic behavior. Fig. 6 shows how the inertia of the rotor/nacelle assembly is modeled. To consider the real dimension of the nacelle, the mass is assigned to an additional joint (the red joint in Fig. 6a) that is connected to the top part of the tower through a rigid link. In this study, the nacelle barycenter is considered perfectly aligned with the tower axis ($ex = 0$ m) and a vertical offset is considered ($ez = 2$ m). Additionally, the inertia characteristics of the rotor need to be defined. For this, the mass of the blade needs to be known; for a fiberglass blade with a length (r_b) of 35 m, a mass (m_b) of about 3.36 ton is expected according to available empirical relationships for the blade length and the blade weight.² Once the blade mass is known, the distance between the center of mass of the nacelle and the center of mass of the rotor should be defined. In

this study, an eccentricity (ex_b) of 3 m is considered (a half of a hypothetical nacelle long 6 m perfectly aligned with the axis of the tower). Assuming that the mass of each blade is uniformly distributed (Fig. 6b) and the three blades are equally spaced at angle 120°, the moments of inertia of the blades, to apply to the central joint (the red node in Fig. 6a) with respect to the three axes, are:

$$I_x = m_b \cdot r_b^2 \tag{5}$$

$$I_y = 0.5 \cdot m_b \cdot r_b^2 + 3 \cdot m_b \cdot ex_b^2 \tag{6}$$

$$I_z = 0.5 \cdot m_b \cdot r_b^2 + 3 \cdot m_b \cdot ex_b^2 \tag{7}$$

2.2.5. Load modeling

Five actions should be considered: (a) the structural self-weight, (b) the hydrostatic action of water on the substructure, (c) the hydrostatic action of soil on the foundation, (d) the wind action on the tower, and (e) the seismic action. The self-weight is applied as static force loads to the structural joints discretizing the structure. The hydrostatic actions of water and soil are neglected since globally self-equilibrated.

The wind action is applied as static force loads to the structural joints along the x direction only. This is a very simplified approach since the dynamic force due to the rotor vibrations is neglected. A normal wind profile is considered, i.e. a wind action that is likely to occur during the operational phase. This condition is more realistic when an earthquake occurs, rather than events such as storms or hurricanes. To completely define the wind action, three parameters are needed: (i) the velocity at the hub height v_{hub} , (ii) the rated wind velocity v_r that is the velocity at which the wind turbine generates

² <http://www.compositesworld.com/articles/offshore-wind-how-big-will-blades-get>.

constant power, and (iii) the density of air ρ_{air} , which is typically equal to 1.25 kg/m^3 . For the normal wind profile, v_{hub} is assumed equal to v_r and both equal to 15 m/s , that is a typical value of wind velocity for which most of turbines produce constant power [46]. The wind action is proportional to the wind profile along the tower that is defined according to the relation proposed by ASCE/SEI 07-10 [47]:

$$v(z) = v_{hub} \left(\frac{z}{h_{hub}} \right)^{0.2} \quad (8)$$

where h_{hub} is the vertical distance between the hub center and the sea surface. The velocity is then transformed into horizontal forces through the following equation:

$$F(z) = 0.5 \cdot \rho_{air} \cdot v(z)^2 \cdot A(z) \quad (9)$$

where $A(z)$ is the tributary area evaluated as in Fig. 3b. An additional concentrated wind action is applied at the node representing the center of the rotor/nacelle assembly. The force is evaluated through the formulation by Frohboese and Schmuck [48] (see Arany et al. [49]):

$$F_{hub} = 0.5 \cdot \rho_{air} \cdot v_{hub}^2 \cdot A_{swept} \cdot C_T \quad (10)$$

where A_{swept} is the swept area shown in Fig. 3a, and C_T is:

$$C_T = 3.5 \cdot v_r \cdot (2 \cdot v_r + 3.5) \cdot \frac{1}{v_{hub}^3} \quad (11)$$

A more refined approach for the application of the wind load is described in Avossa et al. [50].

Finally, the earthquake action is modeled through the application of unscaled strong motions records, described in detail in the following section, at the constrained nodes of the model. In contrast to the self-weight and wind actions, the earthquake is modeled in a dynamic regime by performing NDA. NDA are performed by considering three components of the strong motion records (two horizontal and one vertical). In the past studies, vertical components are often neglected, whilst Kj rslaug and Kaynia [51] emphasized the necessity of considering the vertical motion since they observed that for an inland wind turbine the vertical acceleration between the base and the top of the structure can be amplified by a factor of about 2–6. A larger horizontal component having the higher value of PGA is applied along the x direction that is the direction along which the wind is also applied. It is important to note that in this study, for the model M1 (i.e. the model in which the geotechnical part is explicitly considered), time histories that are applied to all supports along the foundation pile are identical. This assumption can lead to a potential underestimation of the effects, especially for layered soils [15]. Indeed, it is well known that the passage of seismic waves through the soil surrounding a pile imposes curvatures on the pile and therefore additional ‘kinematic’ bending moments [52]. For the analyzed case study, given the absence of refined geotechnical information about the stratigraphy, it is neither possible to model a free-field soil column linked to the spring nor to perform a site response analysis to obtain the modified accelerograms at the foundation support nodes using the bedrock motion. However, results are considered still valid given the short length of the embedded monopile, and given the low aspect ratio of the foundation (embedded length over pile diameter); it has been shown that for the aspect ratio of the pile less than 5 (the examined case study is $15/3.5 \approx 4.3$) the kinematic contribution is negligible [53,54].

Sources of damping for offshore wind turbines include aerodynamic (generally lower than 3.5% [55]), hydrodynamic (generally lower than 0.15% [3]), structural (varying from 0.2% to 0.3% [3,56]), and soil damping. In addition, in some cases tuned mass dampers are also installed at the nacelle [57]. By accounting for the above-mentioned contributions, a Rayleigh damping model is adopted with constant damping of 3% for the 1st and 6th vibration modes; this is analogous to the conventional choice of the 1st and 3rd modes for ordinary structures since the first six modes are almost coincident in pairs (i.e. 1st and

2nd, 3rd and 4th, 5th and 6th). Obviously, potential issues associated with overdamping can occur for higher modes if those are relevant, i.e. if they are associated with high participation masses. Future research should focus on the adoption of different damping models, such as the modal damping scheme [58], so that each mode can be coupled to a different damping value according to more accurate site-specific geotechnical assessment.

2.3. Limit states

A limit state is a condition beyond which the structure-foundation assembly will no longer satisfy the specified performance requirements. According to the DNV guidelines [4], four limit states are conventionally analyzed for offshore wind turbines: (a) the Ultimate Limit State (ULS), (b) the Fatigue Limit State (FLS), (c) the Accidental Limit State (ALS), and (d) the Serviceability Limit State (SLS).

The ULS is related to the maximum load-carrying resistance, and can be reached for several reasons: (i) excessive yielding and/or buckling (i.e. loss of structural resistance); (ii) a failure of a component (e.g. brittle fracture of connections); and (iii) a loss of static equilibrium of the structure (whole or part) with a consequent mechanism (e.g. rigid body behavior, overturning, and capsizing). The FLS is related to cumulative damage due to repeated loads. The ALS considers potential accidental loads (e.g. vessel impact) that can lead to loss of global or local structural integrity. The SLS corresponds to tolerance criteria associated with the regular and normal use of the wind turbine, including: (i) excessive deflection leading to the second order effects modifying the distribution of loads between supported and supporting structures; (ii) excessive vibration jeopardizing the functioning of the non-structural components; (iii) displacements that exceed the limitation of the equipment; (iv) differential settlements of foundation and soil causing intolerable tilt of the wind turbine; and (v) temperature-induced excessive deformations.

In this study, SLS and ULS are considered; such limit states are analyzed with respect to the seismic action, which is the main focus. For each limit state, the capacity (C) and the demand (D) are defined, and the demand over capacity ratio ($Y = D/C$) is studied as a seismic performance metric. The SLS is reached when the maximum chord rotation (i.e. the demand) exceeds 0.5 degrees (i.e. the capacity). The capacity value of 0.5 degrees corresponds to the maximum rotation for which the turbine is switched off [4]. The ULS is checked according to the prescription reported in the Part1-6 of the Eurocode 3 [59] that is the part related to the strength and stability of shell structures. In particular, the Annex D of the previous document is used to calculate the design buckling stress for unstiffened cylindrical and truncated conical shells. Specifically, structural checks are performed based on two formulations: the von Mises equivalent design stress and the buckling strength check through stress limitation.

The von Mises equivalent stress (σ_{eq}) is adopted as follows:

$$Y = D/C = \sigma_{eq}/f_y = \sqrt{\sigma^2 + 3 \cdot \tau^2}/f_y \leq 1 \quad (12)$$

where σ and τ are the meridional stress and the shear planar stress (Fig. 3d), respectively. σ values are automatically obtained as output of OpenSees for each point monitored along the perimeter and height. τ values are obtained as the sum of shear (τ_{shear}) and torsional ($\tau_{torsional}$) stresses. Such stresses are obtained from the global internal stress according to mechanic’s relationships for thin circular hollow sections (i.e. Jourawski theory for shear and Bredt theory for torsion [60]):

$$\tau_{shear} = \frac{\sqrt{V_x^2 + V_y^2} \cdot \sin \alpha}{\pi \cdot t \cdot r} \quad (13)$$

$$\tau_{torsion} = \frac{M_T}{2 \cdot \pi \cdot t \cdot r^2} \quad (14)$$

where V_x , V_y , and M_T are the internal shear forces in the two horizontal

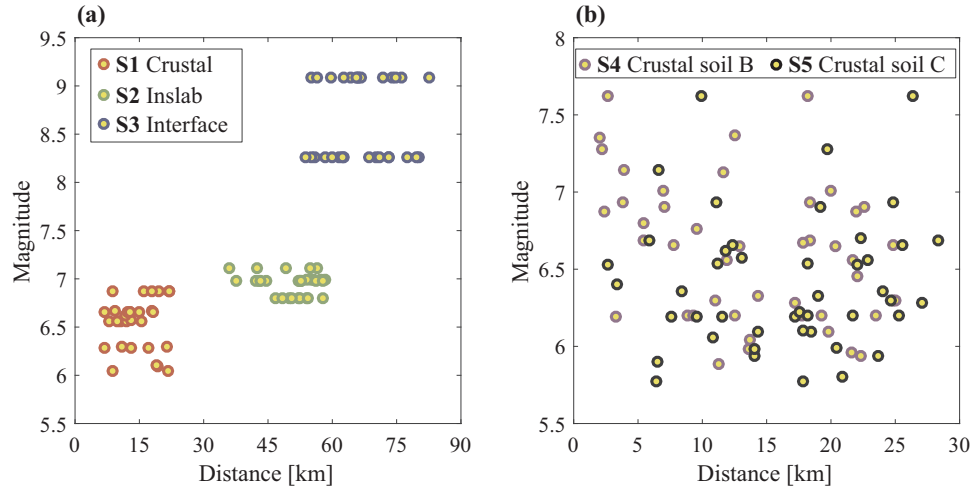


Fig. 7. Magnitude and distance characteristics for (a) Japanese crustal, inslab, and interface records (S1, S2, S3), and for (b) global crustal earthquakes recorded on soil B and C (S4 and S5).

directions and the torsional moment, respectively; α is the angle between the internal total shear vector and the point in which the internal stress is calculated. Finally, r and t are the radius and the thickness of the section, respectively.

For the buckling strength limitation, the following relation is adopted:

$$Y = \left(\frac{\sigma}{\sigma_{x,Rd}} \right)^{k_x} + \left(\frac{\tau}{\tau_{x\theta,Rd}} \right)^{k_\tau} \leq 1 \quad (15)$$

where $\sigma_{x,Rd}$, $\tau_{x\theta,Rd}$, k_x , and k_τ are calculated according to the code suggestions presented in the Part1-6 of the Eurocode 3 [59]. The overall ULS demand over capacity ratio, as also suggested by Winterstetter and Schmidt [61], is the maximum between the two values obtained using Eqs. 12 and 15.

2.4. Analysis cases

Two kinds of analysis are performed; a modal analysis is conducted to understand the dynamic behavior of the different configurations of wind turbine structures, whereas NDA is performed to evaluate the seismic performance quantitatively. Results from NDA are interpreted through the cloud analysis approach, which is based on a probabilistic linear regression model [62]. It allows building fragility curves according to the following formulations:

$$P(Y > 1|IM) = \Phi \left(\frac{\log \eta_{Y|IM}}{\beta_{Y|IM}} \right) \quad (16)$$

$$\log \eta_{Y|IM} = \log a_1 + a_2 \cdot \log IM \quad (17)$$

$$\beta_{Y|IM} = \sqrt{\frac{\sum_{i=1}^n (\log Y_i - \log \eta_{Y|IM})^2}{n - 2}} \quad (18)$$

where IM is the intensity measure adopted to represent the accelerograms employed in the NDA, and typically is the spectral acceleration corresponding to the first period of vibration, i.e. $S_a(T_1)$; n is the number of NDA (i.e. the number of accelerograms). The geometric mean of the spectral accelerations corresponding to the first period of vibration in the two horizontal directions, is adopted as IM:

$$S_a = \sqrt{S_{a,x}(T_{1,x}) \cdot S_{a,y}(T_{1,y})} \quad (19)$$

The records adopted in this study are gathered from two sources: the first one is the strong motion database developed by Foulser-Piggott and Goda [63], where 864 high-quality digital recordings from the K-NET, KiK-net, and SK-net in Japan are available, and the other is a

collection of 379 records from the PEER-NGA database that contains many records from shallow crustal earthquakes globally. The ground motion records (each record consisting of three components) that are compiled for this study satisfy the following selection criteria: (i) the earthquake magnitude is greater than 5.5, (ii) PGA is greater than 0.1 g, and (iii) peak ground velocity is greater than 10 cm/s. All records are properly processed for the long-period ranges (reliable up to 10 s) using the procedure suggested by Boore [64]. Notably, records from Japanese strong motion networks can be characterized by their earthquake types, i.e. crustal, inslab, and interface. Overall, a thorough investigation of the seismic performance of monopile-supported offshore wind turbines subjected to strong motion records of different earthquake types and record characteristics is innovative and distinguishes this study from the past studies. In this study we neglected the potential distinction between pulse-like and non-pulse-like earthquakes.

Five sets of strong motion records are considered in this study. The first three sets are composed of thirty Japanese records each; S1, S2, and S3 are composed of crustal, inslab, and interface subduction earthquakes, respectively. The analysis of the three record types facilitates the comparison of the seismic demand potential of extreme events, such as interface earthquakes that have a very long duration and tend to present high spectral acceleration at long vibration periods [65]. Fig. 7a shows ranges of magnitude and distance values for the selected records belonging to S1, S2, and S3. S4 and S5 are composed of global crustal records composed of Japanese and PEER-NGA databases. The adoption of records covering a large part of the globe is useful for understanding the seismic behavior of the analyzed structural systems more broadly. Both sets are composed of forty-five records; the difference between S4 and S5 is the site classification according to Eurocode 8 [66]: S4 is representative of Soil Class B ($360 \text{ m/s} \leq V_{S30} < 800 \text{ m/s}$), while S5 is for Soil Class C ($180 \text{ m/s} \leq V_{S30} < 360 \text{ m/s}$). Fig. 7b shows ranges of magnitude and distance values for S4 and S5; it is possible to observe that event characteristics of the two sets in terms of magnitude and distance distribution are similar (see Appendix). Although S4 and S5 are representative of different soil profiles in terms of shear wave velocity, the structural and geotechnical models are kept the same in order to obtain insight with regard to the sensitivity of the structural system only to different types of seismic excitations.

Fig. 8 shows the median and the 16th and 84th percentiles of the response spectra for the five sets of accelerograms. It is worth noting that for periods greater than 1 s (i.e. the region of interest for wind turbines, see Fig. 2), for the first three sets, the interface records present the highest values of spectra acceleration for all three components

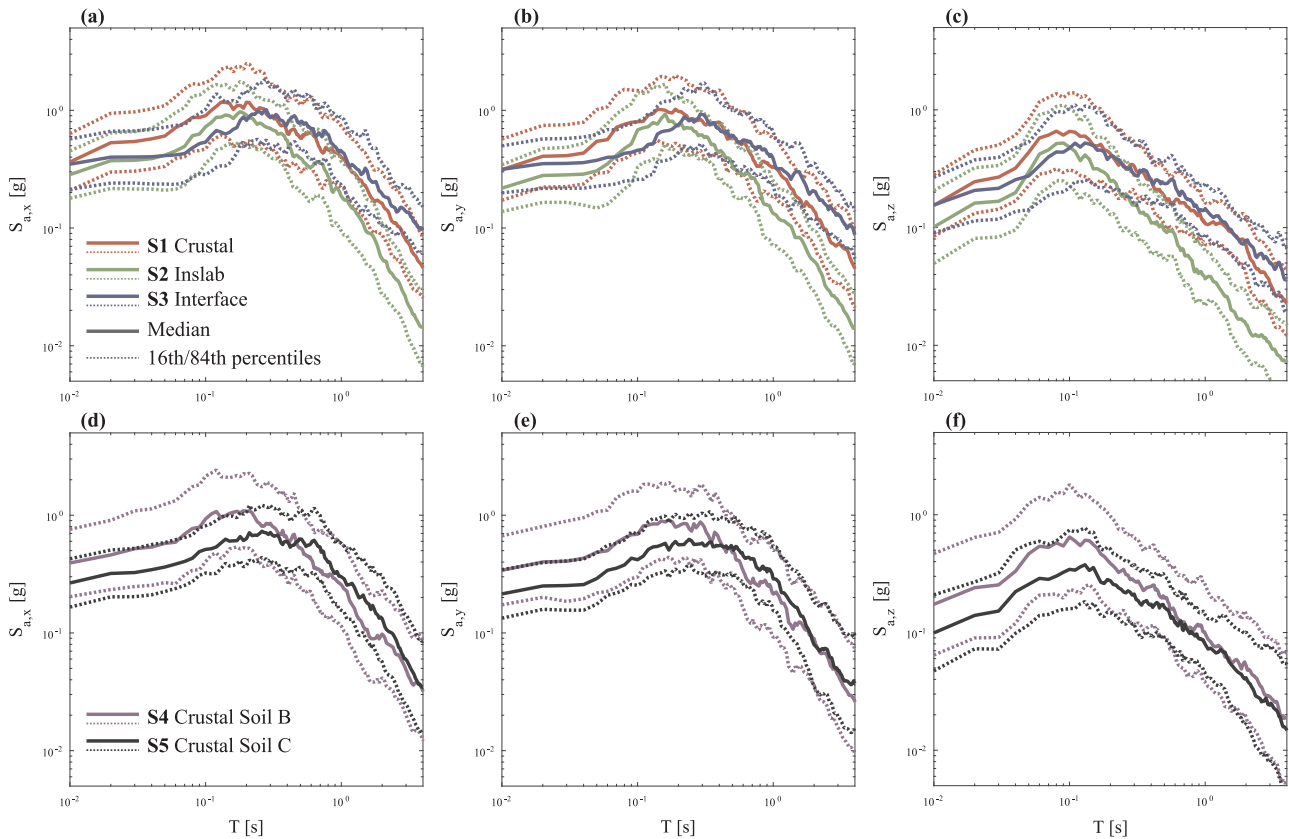


Fig. 8. Median response spectra and confidence interval for (a, b,c) S1, S2, S3, and for (d, e,f) S4 and S5. Spectra related to the (a, d) x, (b,e) y, and (c, f) z directions.

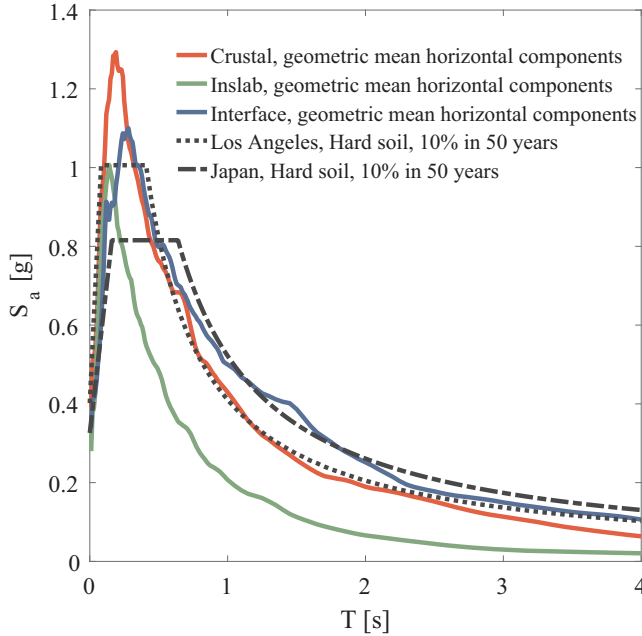


Fig. 9. Geometric mean of the horizontal spectra for S1, S2, S3, and uniform hazard spectra for Los Angeles and Japan.

(Fig. 8a-c), followed in order by the crustal records and then inslab records; in the same region of periods, the signals recorded on soil C present higher spectral acceleration with respect to the ones recorded on soil B, especially for the horizontal components. In terms of dispersion around the median, the first three sets present comparable variability (logarithmic standard deviation β of about 0.62 for S1 and S2 and 0.52 for S3), whilst the crustal earthquakes recorded on soil B

Table 2

Structural models (NWB: nonlinear Winkler beam; IF: impedance functions; FR: fixed restraint; ND: non-degrading in compression; D: degrading in compression).

	M1	M2	M3	M4	M5	M6
SSI	NWB	IF	FR	NWB	NWB	NWB
Door	no	no	no	along y	along x	no
Material	ND	ND	ND	ND	ND	D

presents higher variability ($\beta = 0.89$) with respect the ones recorded on soil C ($\beta = 0.74$).

It is worth noting that Japanese record sets have response spectra that on average match the uniform hazard spectra of active seismic regions, such as Japan and the US, in the typical range of principal vibration periods of wind turbines. Fig. 9 shows for example the overlay of the average spectra of S1, S2, and S3 with the uniform hazard spectra (corresponding to a probability of 10% in 50 years) for Japan and for Los Angeles obtained according to Kuramoto [67] and ASCE 7–10 [47], respectively. It is possible to observe that the code-based Japanese spectrum matches very well the mean spectrum of the interface records, meanwhile the code-based US spectrum matches the mean spectrum of the crustal records. Therefore, although adopted records are representative of extreme events recorded up to now, such strong motions are probabilistically ‘anticipated’ at locations of future construction of offshore wind turbine farms in active seismic regions.

2.5. Analysis setup

Six different structural models M1 to M6, obtained combining different modeling options, are analyzed in the following. Table 2 shows the matrix of structural models that are analyzed. M1, i.e. the model without entrance door, with non-degrading material in compression and having the foundation modeled as nonlinear Winkler beam, is used

Table 3
Influence of SSI on modal analysis. (T: vibration period; M: modal participation mass).

Mode	T [sec]			Mx [%]			My [%]			Mz [%]		
	M1	M2	M3	M1	M2	M3	M1	M2	M3	M1	M2	M3
1	2.301	1.936	1.928	–	–	–	21.9	44.1	43.9	–	–	–
2	2.295	1.929	1.921	22.0	44.4	44.2	–	–	–	–	–	–
3	0.414	0.340	0.338	–	–	–	12.1	16.5	15.9	–	–	–
4	0.399	0.322	0.319	12.8	17.5	16.8	–	–	–	–	–	–
5	0.185	0.144	0.143	–	–	–	10.2	11.2	10.1	–	–	–
6	0.171	0.129	0.127	11.0	12.0	10.7	–	–	–	–	–	–
7	0.107	0.081	0.078	–	–	–	8.5	10.9	9.50	–	–	–
8	0.097	0.075	0.073	8.5	9.60	8.30	–	–	–	–	–	–
9	0.080	0.069	0.069	–	–	–	–	–	–	59.0	73.8	79.4

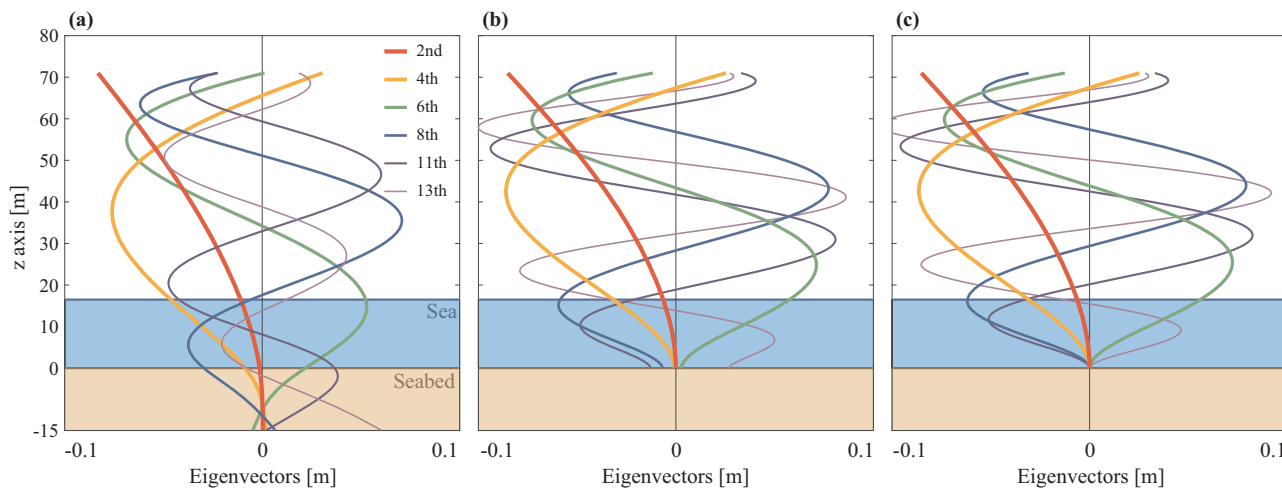


Fig. 10. First six normalized eigenvectors along the x direction for models (a) M1, (b) M2, and (c) M3.

Table 4
Influence of the door on modal analysis. (T: vibration period; M: modal participation mass).

Mode	T [sec]			Mx [%]			My [%]			Mz [%]		
	M1	M4	M5	M1	M4	M5	M1	M4	M5	M1	M4	M5
1	2.301	2.307	2.313	–	22.0	–	21.9	–	21.8	–	–	–
2	2.295	2.302	2.295	22.0	–	22.0	–	21.9	–	–	–	–
3	0.414	0.414	0.415	–	–	–	12.1	12.1	12.2	–	–	–
4	0.399	0.399	0.399	12.8	12.9	12.8	–	–	–	–	–	–
5	0.185	0.185	0.186	–	–	–	10.2	10.2	10.1	–	–	–
6	0.171	0.174	0.174	11.0	10.9	11.0	–	–	–	–	–	–
7	0.107	0.107	0.107	–	–	–	8.5	8.5	8.4	–	–	–
8	0.097	0.097	0.097	8.5	8.5	8.5	–	–	–	–	–	–
9	0.080	0.080	0.080	–	–	–	–	–	–	59.0	58.9	58.9

as reference to study the sensitivity to the five sets of accelerograms. M1, M2 and M3, having different foundation assumptions, are compared by considering only the crustal Japanese records (S1). The same set of accelerogram is used to compare M1 with M4 and M5 that are models having the entrance door at the base aligned along the x and y directions, respectively. The door is 1.6 m wide and 2.2 m tall, and is located at 2 m from the sea level. Finally, S1 is used to study the response of M1 with respect to M6, in which the material degradation in compression is modeled.

3. Results

3.1. Modal analysis

A preliminary modal dynamic analysis is performed for M1 to M5; M6 is not analyzed since it is identical to model M1 except for the

nonlinear behavior, which does not affect the modal dynamic analysis. Table 3 shows a comparison between M1, M2 and M3 (i.e. three models representing different ways of implementing SSI). It can be observed that the first period of vibration is around 2 s, which is in agreement with the measured frequency of about 0.5 Hz reported in Arany et al. [23] for the case study structure. Specifically, the implementation of the foundation through the NWB slightly increases the vibration periods with respect to the IF and FR cases. On the other hand, the participation masses of M2 and M3 associated with the first vibration mode are higher than the corresponding participation mass of M1. It is worth noting that for M1, the participation mass is almost uniformly spread among several modes, and 14 vibration modes are required to have exactly 100% of participation masses in both horizontal directions (7 pure translational modes for each direction). Conversely, for M2 and M3, the 100% of participation mass along the horizontal direction is reached with 22 vibration modes, i.e. 11 pure translational modes for

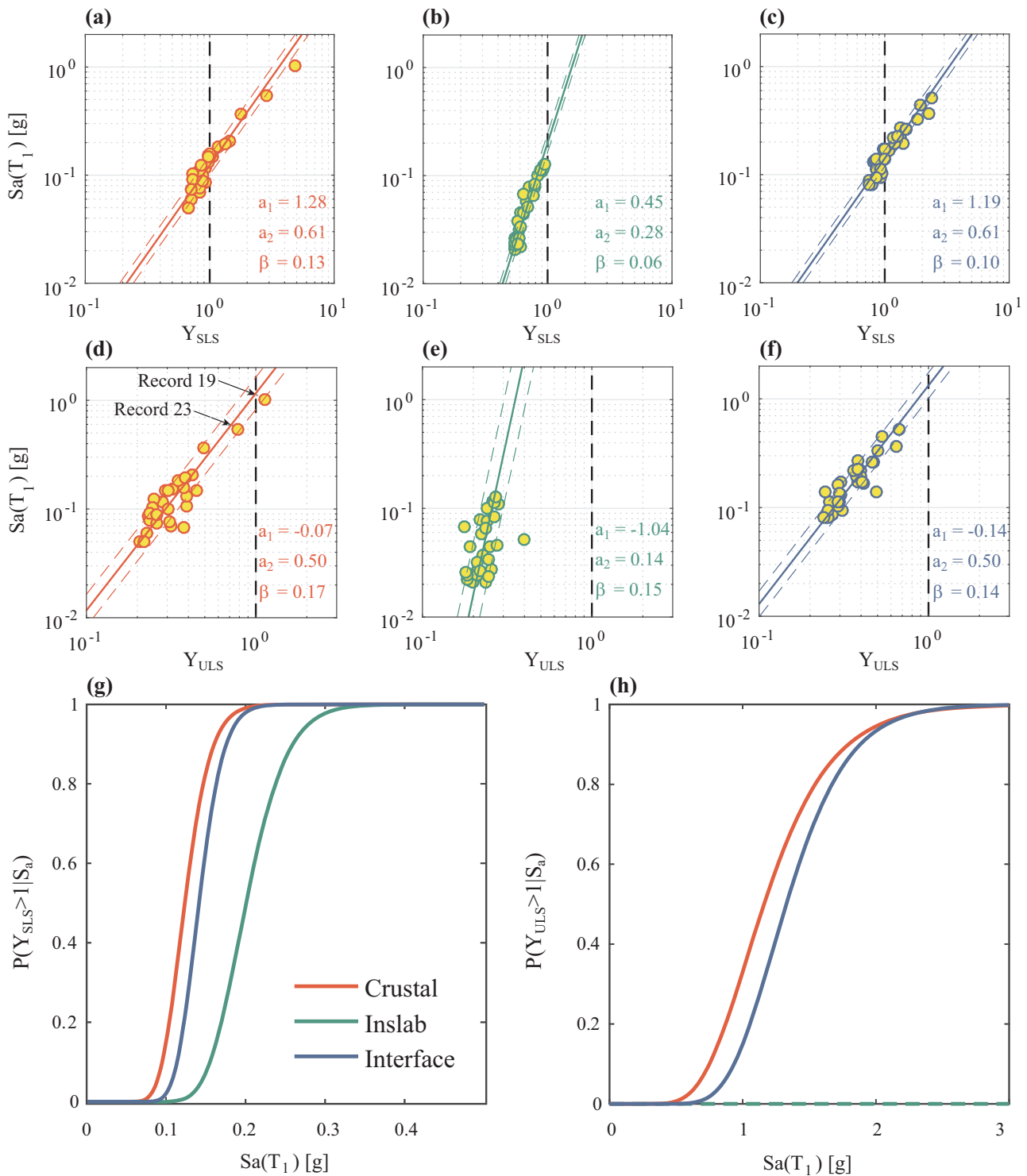


Fig. 11. Cloud analysis results for M1 subjected to Japanese (a, d) crustal, (b, e) inslab and (c, f) interface records, respectively. Results related to (a-c) SLS and (d-f) ULS. Fragility curves for different earthquake types for (g) SLS and (h) ULS. The ULS fragility curve for inslab earthquakes cannot be calculated, therefore it is represented as broken line.

each direction. It is worth nothing that the adoption of the Rayleigh damping scheme for the NDA can lead to an overdamping of higher modes; therefore, even if a high number of modes is required to reach the 100% of the participation mass, the influence of higher modes is reduced by the potential high value of damping. Fig. 10 shows the first six normalized eigenvectors for M1, M2, and M3. It is observed that the eigenvectors for M1 (Fig. 10a) involve the foundation that is explicitly modeled, meanwhile for M3, displacements and rotations are fixed (Fig. 10c); eigenvector shapes for M2 (Fig. 10b) are between M1 and

M3.

The difference between the modal behavior of M1 and M2 is due to both the different modeling approach and the assumed soil properties. In fact, M1 assumes distributed springs with stiffness linearly increasing with depth, while M2 stiffness increase parabolically with depth.

Table 4 shows a comparison of M1 with M4 and M5 (i.e. models with the door opening at the base oriented along the y direction (M4) reducing the stiffness of the x direction, and along the x direction (M5) reducing the stiffness of the y direction). It is possible to observe a slight

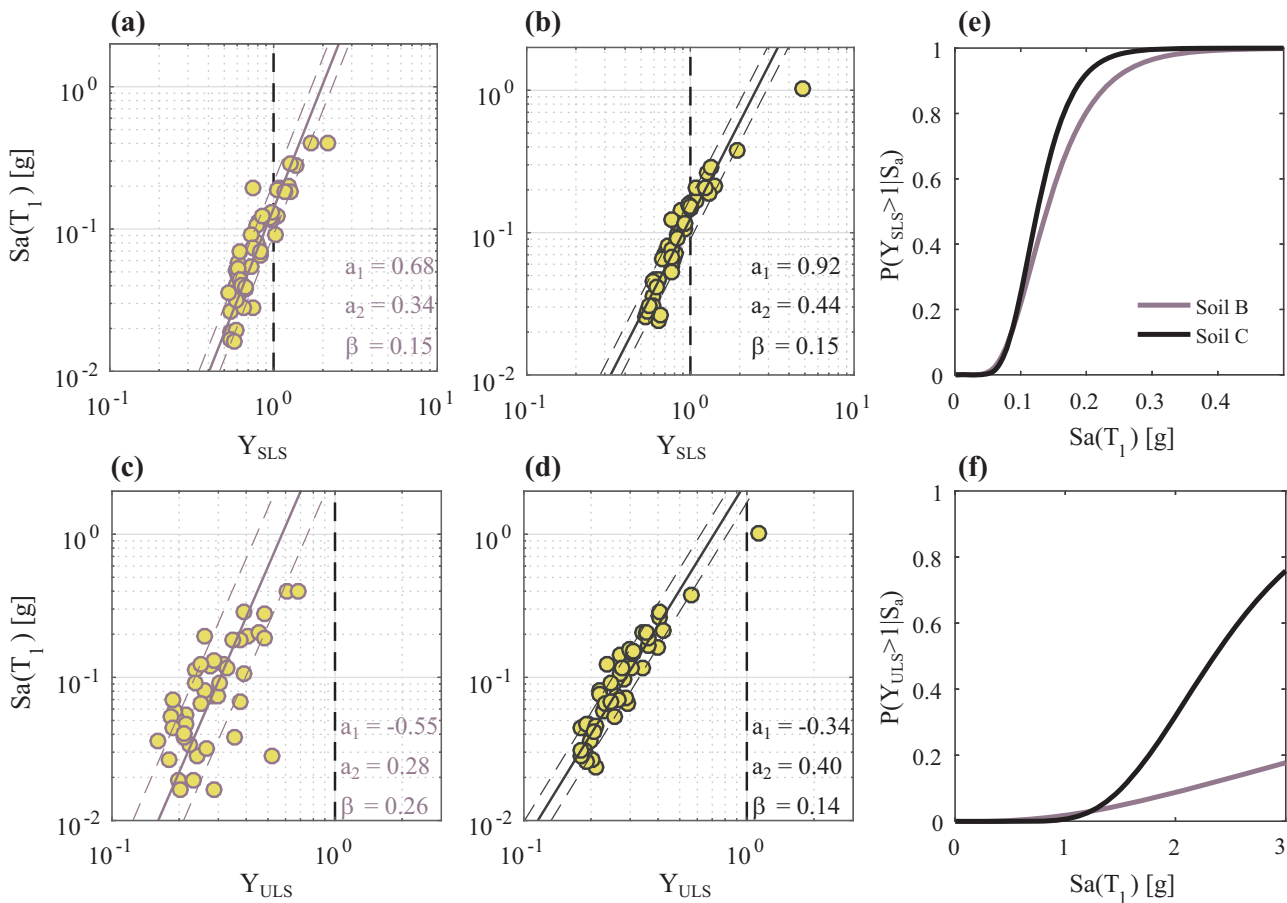


Fig. 12. Cloud analysis results for M1 subjected to (a, c) S4 and (b, d) S5, respectively. Results related to (a-b) SLS and (c-d) ULS. (e) SLS and (f) ULS fragility curves obtained for S4 and S5.

increase in the first vibration period and an (expected) change of direction of the first mode for M4 with respect to M1. No variations for the higher vibration modes are observed.

It is worth mentioning that in the aftermath of a seismic event, phenomena of period elongation can occur due to the damage incurred by the structure and the soil. The period elongation is generally due to the reduction of stiffness. On the other hand, the cyclic interaction between the foundation and the soil can lead to a dynamic “consolidation” of the soil with a consequent hardening and therefore a reduction of the vibration period.

3.2. Nonlinear dynamic analysis

As explained in Section 2.4, fragility curves are developed using the cloud method. Such a method performs well for the SLS; unfortunately, few collapses are observed and therefore ULS fragility curves rely on the linear extrapolation only. Therefore, fragilities related to the ultimate conditions should be considered as preliminary results, and more comprehensive methods, such as IDA [68] or multiple-stripe method should be adopted to investigate the collapse case.

3.2.1. Sensitivity to earthquake record characteristics

Fig. 11 shows NDA results for S1, S2 and S3. Specifically, Fig. 11a-f shows the demand over capacity ratio for both SLS (Fig. 11a-c) and ULS (Fig. 11d-f). In terms of SLS, several crustal and interface records lead to the attainment of the limit state; by contrast, none of inslab records reach the SLS. In terms of ULS, only one crustal record causes a structural failure for $Sa(T_1)$ equal to about 1 g (Event 19 in Table A1), meanwhile another one leads the structure to 80% of its capacity for $Sa(T_1)$ of about 0.8 g (Event 23 in Table A1). These two earthquakes are

recorded at stations close to the seismic source and on deformable soils. These two events that present high values of spectral acceleration for a long vibration period can be considered extreme events for the considered structure.

Fig. 11g-h shows the fragility curves obtained from linear regression. It is possible to observe that, for both limit states, the structure is more sensitive to crustal records and less sensitive (or completely insensitive) to inslab records. Interface records induce structural demands that are very close to crustal records for both limit states. The similarities between crustal and interface fragilities can be explained by the modal behavior of the analyzed structure and by the spectral characteristics of the two record sets. In fact, Table 3 shows that participation masses are almost equally distributed between vibration modes with period longer and shorter than 0.4 s. Periods longer than 0.4 s correspond to the period range of the two principal translational vibration modes where the median spectrum of the interface records is higher than the spectrum of crustal records. Periods shorter than 0.4 s are within the range of higher modes, where the crustal spectra are higher than interface spectra. The slightly higher vulnerability to crustal records makes clear that the higher modes are important for the vulnerability assessment of wind turbine structures.

3.2.2. Sensitivity to records frequency content due to different soil type

In this section, NDA results corresponding to S4 and S5 are discussed. Fig. 12a-d shows the demand over capacity ratio for the SLS (Fig. 12a-b) and for the ULS (Fig. 12c-d), and Fig. 12e-f shows the associated fragility curves. It is observed that structures on softer soils are more affected than structures on stiffer soils. Also in this case the observed tendencies of the results can be explained by noting the key features of spectral shapes of the records; in fact, the higher sensitivity

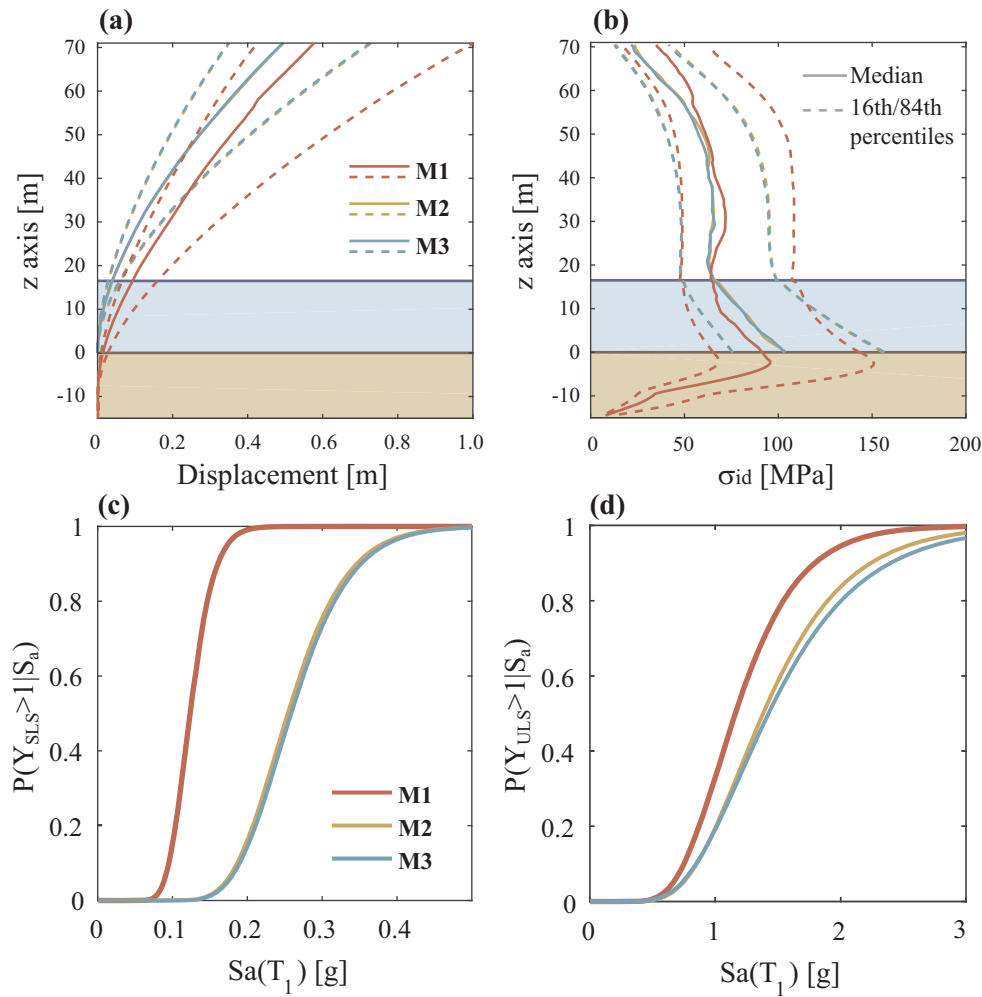


Fig. 13. (a) Displacement and (b) equivalent stress for M1, M2, and M3 subjected to S1. (c) SLS and (d) ULS fragility curves for M1, M2, and M3 subjected to S1.

to S5 reflects that higher values of median spectrum of S5 in the range of vibration periods of interest for the wind turbine (i.e. greater than 0.4 s). It is also worth noting that the larger variability of spectra for S4 is reflected in the larger variability of the ULS fragility curve with respect to the fragility for S5.

It is important to emphasize the comparison between these two sets of crustal accelerograms with the set S1 that has only Japanese crustal records. The SLS fragility curves derived using S1, S4 and S5 are similar; the latter two differ from the one obtained with S1 for a slightly higher variability, reflecting the higher variability of the input record sets. On the contrary, the ULS fragility curves for S4 and S5 show a lower vulnerability with respect to the fragility obtained for S1. This is because both S4 and S5 are composed of accelerograms recorded at global scale and the average spectra are generally lower than the one related to the Japanese crustal records, especially for higher-mode sensitive periods.

It is important to underline that the obtained results are valid under the assumption that geotechnical parameters have not been varied to reflect the different shear wave velocity profiles. More investigations are needed in future.

3.2.3. Importance of the SSI

Results related to models M1, M2, and M3 subjected to S1 are discussed. Fig. 13 a-b shows the median response in terms of displacement (Fig. 13a) and maximum equivalent stress (Fig. 13b) along the tower height; the 16th and 84th percentiles are also shown in the same figures (dashed lines). M1 presents larger displacements with

respect to M2 and M3 that are almost coincident. This result is due to the higher deformability of M1 due to the more sophisticated soil modeling. In terms of stress, it is possible to observe that on average, equivalent stresses for M1 are higher for the tower and lower for the substructure with respect to M2 and M3. This result is due to the restraint conditions; M2 and M3 induce higher concentrations of stress at the mudline level due to the restrained location. On the other hand, M1 presents lower values of stress since stress induced by the superstructure is gradually distributed along the foundation that is explicitly modeled, noting that the higher deformability of M1 induces higher stresses on the tower. Finally, given the higher deformability, the results of M1 present a higher variability with respect to the results associated with the other two models. Therefore, it is very important to model the foundation properly in order to have reliable assessment of the stresses along the structure. Moreover, the higher variability due to the soil modeling leads to the necessity of a more refined record selection.

Fig. 13c-d shows fragility curves derived for the three models. Results highlight the importance of implementing SSI in a more refined manner; in fact, simplified restraint modeling leads to an overestimation of the capacity for both limit states. Similar trends on fragility curves were found for bridges piers [69].

3.2.4. Influence of door opening

Fig. 14a-b shows the central values and the confidence intervals of the response in terms of displacement (Fig. 14a) and maximum equivalent stress (Fig. 14b) along the vertical axis. No differences in

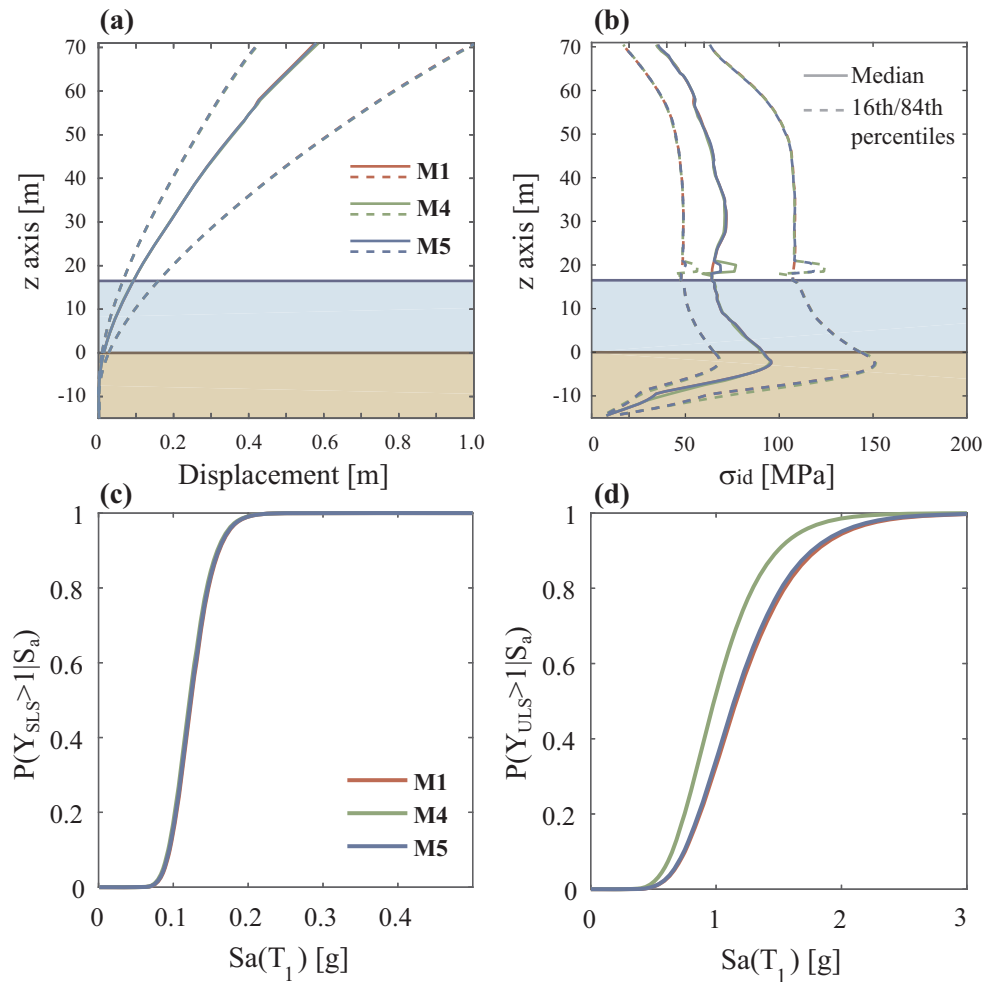


Fig. 14. (a) Displacement and (b) equivalent stress for M1, M4, and M5 subjected to S1. (c) SLS and (d) ULS fragility curves for M1, M4, and M5 subjected to S1.

terms of displacement can be observed for the three models M1, M4 and M5. Conversely, an increase of equivalent stress is observed where the door is located. M4 presents the highest level of stress increase. Such results in terms of displacement and internal stress are reflected in fragility curves (Fig. 14c-d); in fact, fragilities corresponding to the SLS are almost identical for the three analyzed models, meanwhile, fragilities corresponding to the ULS present greater differences. Specifically, models with door opening are more vulnerable with respect to the model without the door, especially when the door is aligned orthogonally to the main loading axis (i.e. M4).

3.2.5. Effect of the material degradation

The effect of material degradation becomes significant only if the yield stress in compression is reached. For the examined case study, only two records (i.e. the two points in the dashed circles in Fig. 15a-d) cause seismic demands exceeding the yield stress level. These two records have a high level of spectral acceleration and induce the flexural yielding of the structure. Moreover, it is observed that when the equivalent stress is about 90% of the yielding stress, the failure progresses abruptly from yielding to buckling. Variation for the two records has no significant effects on both limit states in terms of fragility curves (Fig. 15e-f). Obviously, the result obtained for the specific case study cannot be generalized; the degrading behavior in compression should be modeled more accurately when detailed experimental information on the mechanical behavior in compression of the adopted steel shell structure is available.

4. Summary and conclusions

This paper presented an analytical procedure to evaluate the seismic assessment of steel monopile-supported offshore wind turbines, which is a structural typology commonly adopted in seismic-prone countries investing in offshore wind power farms. Modeling details about the structure, foundation, material, inertia, and loading are provided and a finite element model was developed through the open-source structural software OpenSees. Important aspects in the modeling, such as different soil structure interaction modeling approaches, different material behavior and the influence of door opening at the tower base, were also investigated. Models were analyzed through non-linear dynamic analyses using five record sets of input ground motions, that facilitated the comprehensive assessments of the influence of the earthquake types and the soil deformability. Two limit states were considered for the assessment: the serviceability limit state, reached when the chord rotation exceeded 0.5 degrees, and the ultimate limit state, reached when either yielding or local buckling occurs. Based on the thorough analyses of the seismic performance, represented in the paper using seismic fragility functions, the following conclusions can be drawn:

1. The analyzed structural typology is particularly sensitive to extreme crustal and interface records;
2. Higher modes are not negligible, especially if the SSI is explicitly modeled;
3. Frequency content of records associated to deformable soil induces an increased seismic fragility with respect to stiffer soil;

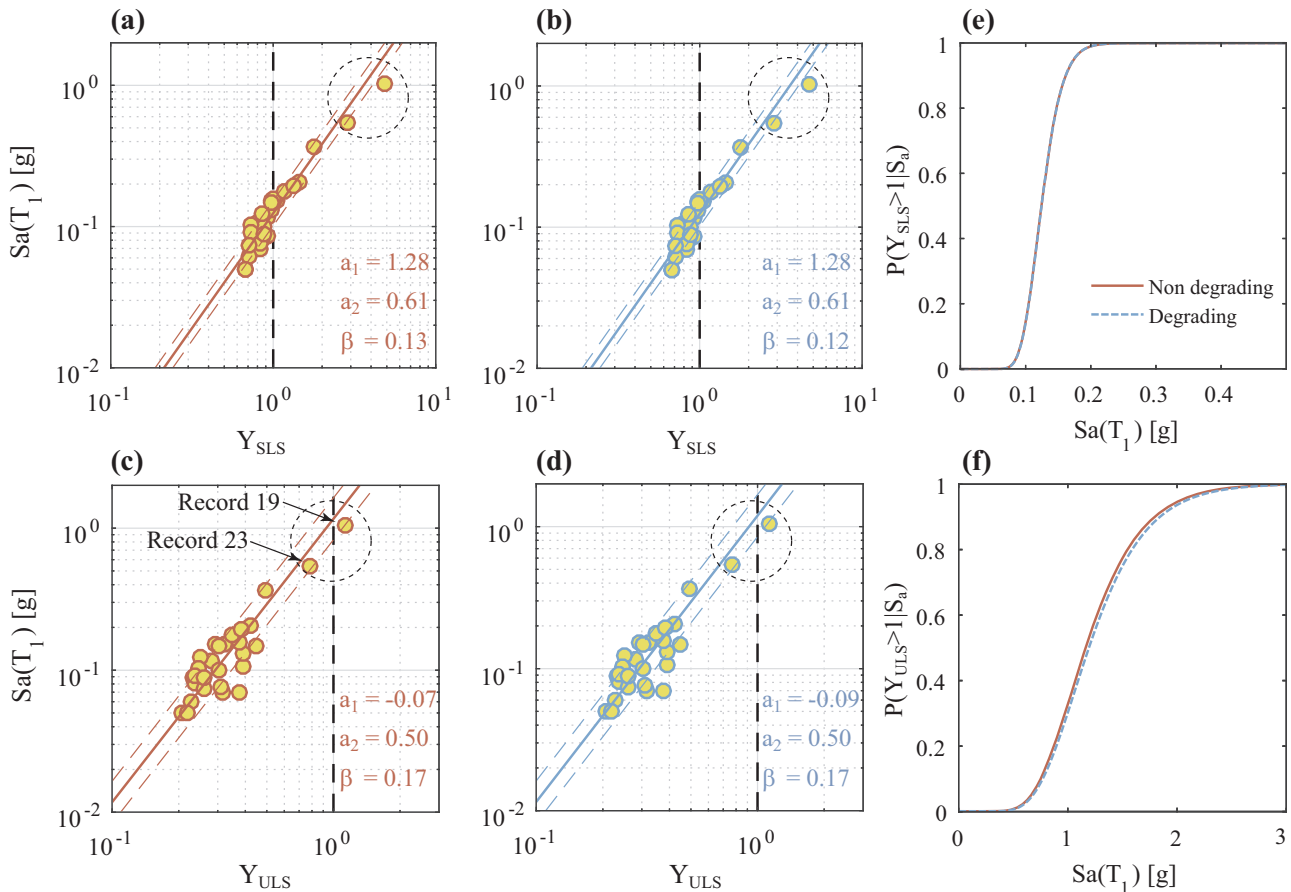


Fig. 15. Cloud analysis results for (a, c) M1 and (b, d) M6 subjected to S1. Results related to (a-b) SLS and (c-d) ULS. (e) SLS and (f) ULS fragility curves subjected to S1 considering and neglecting material degradation in compression.

4. The lack of a proper SSI modeling leads to an overestimation of the seismic capacity of about 60% and 70% for the SLS and ULS, respectively, therefore accurate nonlinear models considering also a proper kinematic interaction for the foundation are needed;
5. The modeling of the door opening at the tower base is essential for a reliable assessment of the ULS because of the stress concentration in that region of the structure; the worst situation is observed when the door is aligned orthogonally to the main direction of environmental loads;
6. It was observed that local buckling can occur; obviously the adoption of a degrading behavior in compression for the material in combination to the corotational formulation is essential to capture potential global buckling mechanisms in the structural analysis;
7. The SLS was frequently reached when subjected to severe strong motions. This is a major issue because the continuity in power generation is essential when the wind turbine represents a component of an energy supply chain or when it is adopted to increase the resilience of an energy network [8]; on the contrary the ULS was rarely attained.

It is important to emphasize that this study is based on numerical results obtained through a new model that goes beyond the classical models adopted in industries and in previous research, but still presents some exemplifications. Therefore, more refined models need to be used for future research, considering a more refined modeling of damping,

explicitly considering the free-field soil column attached to the non-linear springs, and considering the dynamic actions due to the functional state of the wind turbine. A rigorous investigation of sufficient and efficient intensity measure is also required. Finally, it is essential to carry out more thorough incremental dynamic analyses to have a more reliable estimation of the ultimate limit state.

Acknowledgements

The research is funded by the Engineering and Physical Sciences Research Council (EPSRC) grant (EP/M001067/1) for the first author, the EPSRC GCRF (University of Surrey Internal grant) for the second author, and the Leverhulme Trust (RPG-2017-006, GENESIS project) for the third author. Ground motion data for Japanese earthquakes and worldwide crustal earthquakes were obtained from the K-NET and KiK-net database (<http://www.kyoshin.bosai.go.jp/>), the SK-net (<http://www.sknet.eri.u-tokyo.ac.jp/>), and the PEER-NGA database (<http://peer.berkeley.edu/nga/index.html>). This work was carried out using the computational facilities of the Advanced Computing Research Center, University of Bristol (<http://www.bris.ac.uk/acrc/>).

Data availability

All underlying data are provided in full within this paper.

Appendix A

See Tables A1–A5

Table A1

Set S1, Japanese crustal records on soft and stiff soils.

ID	Record ID	Event ID	Magnitude	R [km]	V _{S30} [m/s]
1	5026	142	6.10	19.23	213
2	37117	792	6.65	6.81	167
3	37157	792	6.65	15.07	168
4	37309	792	6.65	12.90	464
5	94472	1512	6.04	21.56	175
6	94476	1512	6.04	8.68	304
7	136605	1927	6.56	10.67	303
8	136607	1927	6.56	7.90	334
9	136608	1927	6.56	9.91	360
10	136609	1927	6.56	15.43	434
11	136840	1927	6.56	11.95	375
12	138196	1929	6.11	18.92	303
13	140627	1937	6.28	6.83	334
14	140629	1937	6.28	17.23	434
15	140839	1937	6.28	12.98	375
16	165123	2218	6.58	13.08	209
17	222649	2782	6.67	17.79	566
18	222652	2782	6.67	9.29	392
19	232727	2910	6.62	11.82	227
20	260133	3196	6.87	19.49	747
21	260134	3196	6.87	22.03	308
22	260165	3196	6.87	21.96	463
23	260166	3196	6.87	16.08	389
24	260365	3196	6.87	18.01	486
25	260367	3196	6.87	8.74	371
26	355758	4144	6.30	11.05	630
27	355951	4144	6.30	21.51	461
28	393116	4359	6.65	12.35	292
29	393119	4359	6.65	12.75	308
30	393419	4359	6.65	18.27	240

Table A2

Set S2, Japanese in-slab records on soft and stiff soils.

ID	Record ID	Event ID	Magnitude	R [km]	V _{S30} [m/s]
1	46715	951	6.80	49.99	258
2	46716	951	6.80	52.08	307
3	46724	951	6.80	54.10	261
4	46754	951	6.80	52.39	166
5	46755	951	6.80	54.38	247
6	46760	951	6.80	46.82	211
7	47012	951	6.80	57.88	268
8	47014	951	6.80	50.59	299
9	47052	951	6.80	48.44	462
10	86726	1403	6.99	55.14	1125
11	86762	1403	6.99	55.63	495
12	86763	1403	6.99	57.15	505
13	87019	1403	6.99	58.24	670
14	87044	1403	6.99	53.97	934
15	153999	2080	6.98	52.37	202
16	154000	2080	6.98	52.12	175
17	154001	2080	6.98	43.01	282
18	154002	2080	6.98	44.63	274
19	154003	2080	6.98	56.24	313
20	154005	2080	6.98	37.68	297
21	154006	2080	6.98	42.06	180
22	154008	2080	6.98	57.92	243
23	154229	2080	6.98	52.65	189
24	154235	2080	6.98	43.31	213
25	154244	2080	6.98	52.55	168
26	388544	4323	7.11	56.47	494
27	388548	4323	7.11	49.08	221
28	388550	4323	7.11	42.44	304
29	388551	4323	7.11	36.04	1437
30	388552	4323	7.11	54.82	436

Table A3

Set S3, Japanese interface records on soft and stiff soils.

ID	Record ID	Event ID	Magnitude	R [km]	V _{S30} [m/s]
1	100600	1581	8.26	70.30	232
2	100607	1581	8.26	73.12	437
3	100608	1581	8.26	61.50	195
4	100609	1581	8.26	55.79	161
5	100613	1581	8.26	77.57	383
6	100614	1581	8.26	58.29	113
7	100615	1581	8.26	71.11	259
8	100618	1581	8.26	80.23	339
9	100619	1581	8.26	68.58	387
10	100620	1581	8.26	55.17	503
11	100631	1581	8.26	60.08	266
12	100871	1581	8.26	53.66	459
13	100941	1581	8.26	73.12	219
14	100946	1581	8.26	79.56	204
15	100947	1581	8.26	62.60	230
16	101018	1581	8.26	62.25	140
17	341093	4093	9.08	66.06	339
18	341099	4093	9.08	71.80	282
19	341100	4093	9.08	82.65	268
20	341136	4093	9.08	64.29	429
21	341137	4093	9.08	65.80	390
22	341138	4093	9.08	66.78	251
23	341382	4093	9.08	65.67	353
24	341393	4093	9.08	62.76	274
25	341397	4093	9.08	76.19	290
26	341398	4093	9.08	55.06	313
27	341808	4093	9.08	59.65	237
28	341813	4093	9.08	73.90	350
29	341866	4093	9.08	74.83	301
30	341869	4093	9.08	56.53	244

Table A4

Set S4, global crustal records, Soil B.

ID	Record ID	Event ID	Magnitude	R [km]	V _{S30} [m/s]
1	126	41	6.80	2.05	767
2	143	46	7.35	14.37	660
3	265	64	6.33	8.83	600
4	300	69	6.20	3.26	489
5	448	90	6.19	9.60	660
6	495	97	6.76	3.85	462
7	753	118	6.93	6.96	514
8	825	123	7.01	2.19	685
9 ^a	879	125	7.28	5.43	526
10 ^a	983	127	6.69	7.08	609
11 ^a	1111	129	6.90	2.69	553
12	1231	137	7.62	3.93	425
13	1617	138	7.14	12.56	724
14	1633	144	7.37	11.66	685
15	1787	158	7.13	9.32	553
16	2632	172	6.20	12.53	553
17	2739	173	6.20	12.90	464
18	37309	792	6.65	13.71	593
19	94627	1512	6.04	11.90	553
20	136841	1927	6.56	11.29	553
21	147829	2005	5.89	2.42	506
22	260366	3196	6.87	11.05	630
23	355758	4144	6.30	7.79	596
24	393118	4359	6.65	13.65	511
25	513988	5754	5.98	22.56	500
26	288	68	6.90	18.41	714
27	810	118	6.93	19.95	457
28	827	123	7.01	18.36	546
29	952	127	6.69	18.16	553
30 ^a	1520	137	7.62	19.30	475
31	2655	172	6.80	2.05	767
32	2703	173	7.35	14.37	660
33	3507	175	6.33	8.83	600
34	5024	142	6.20	3.26	489
35	32628	731	6.19	9.60	660
36	37310	792	6.76	3.85	462

(continued on next page)

Table A4 (continued)

ID	Record ID	Event ID	Magnitude	R [km]	V _{S30} [m/s]
37	136838	1927	6.93	6.96	514
38	140629	1937	7.01	2.19	685
39	222649	2782	7.28	5.43	526
40	260165	3196	6.69	7.08	609
41	296269	3612	6.90	2.69	553
42	355952	4144	7.62	3.93	425
43	365171	4200	7.14	12.56	724
44	393420	4359	7.37	11.66	685
45	400793	4407	7.13	9.32	553

^a stands for pulse-like according to [70].

Table A5

Set S5, global crustal records, Soil C.

ID	Record ID	Event ID	Magnitude	R [km]	V _{S30} [m/s]
1	30	25	6.19	9.58	290
2	160	50	6.53	2.68	223
3	319	73	5.90	6.50	194
4	368	76	6.36	8.41	257
5	458	90	6.19	11.54	222
6	530	101	6.06	10.84	207
7	547	102	5.77	6.39	271
8	558	103	6.19	7.58	271
9	725	116	6.54	11.16	207
10 ^a	766	118	6.93	11.07	271
11	1044	127	6.69	5.92	269
12	1141	134	6.40	3.36	220
13	1595	137	7.62	9.96	259
14	1605	138	7.14	6.58	276
15	5029	142	6.10	14.34	233
16	165123	2218	6.58	13.08	209
17	232727	2910	6.62	11.82	227
18	393116	4359	6.65	12.35	292
19	400560	4407	5.93	14.07	292
20	514157	5754	5.98	14.10	201
21	169	50	6.53	22.03	275
22	214	53	5.80	20.92	271
23	266	64	6.33	18.96	275
24	322	76	6.36	24.02	271
25	412	80	5.77	17.79	257
26	549	103	6.19	17.17	271
27	668	113	5.99	20.42	270
28	718	115	6.22	17.59	207
29	721	116	6.54	18.20	192
30	778	118	6.93	24.82	216
31	848	125	6.19	9.58	290
32	987	127	6.53	2.68	223
33	1116	129	5.90	6.50	194
34 ^a	1484	137	6.36	8.41	257
35	2507	172	6.19	11.54	222
36	2752	173	6.06	10.84	207
37	2057	63	5.77	6.39	271
38	5025	142	6.19	7.58	271
39	29153	687	6.54	11.16	207
40	136610	1927	6.93	11.07	271
41	140630	1937	6.69	5.92	269
42	296044	3612	6.40	3.36	220
43	355757	4144	7.62	9.96	259
44	393115	4359	7.14	6.58	276
45	400559	4407	6.10	14.34	233

^a Stands for pulse-like according to [70].

References

- [1] GWEC, Global Wind Energy Council. Global wind report, 2016 annual market update. Brussels, Belgium; 2017. p. 76. Available at: <http://www.gwec.net/publications/global-wind-report-2/global-wind-report-2016/>. Last access 01 July 2017.
- [2] Giardini D, Grünthal G, Shedlock KM, Zhang P. The GSHAP global seismic hazard map. *Ann di Geofis* 1999;42(6):1225–8.
- [3] Germanischer Lloyd GL. Guideline for the certification of offshore wind turbines. Hamburg, Germany; 2005.
- [4] DNV, Det Norske Veritas. Design of Offshore Wind Turbine Structures. Offshore Standard DNV-OS-J101; 2014. p. 238. Available at: <https://www.dnvgl.com/>.
- [5] IEC, International Electrotechnical Commission. IEC 61400-3: Wind Turbines – Part 3: Design Requirements for Offshore Wind Turbines, 3rd ed.; 2009.
- [6] Swan S, Hadjian AH. The 1986 North Palm Springs earthquake: effects on power facilities. NP-5607 Research Project 2848, Electric Power Research Institute (EPRI), Palo Alto, CA; 1988. Available at: <https://www.epri.com/#/pages/product/NP-5607>.

- 5607/0. Last access: 01/09/2017.
- [7] Butt UA, Ishihara T. Seismic load evaluation of wind turbine support structures considering low structural damping and soil structure interaction. *Eur Wind Energy Assoc Annu Event* 2012;16–9.
- [8] Bhattacharya S, Goda K. Use of offshore wind farms to increase seismic resilience of Nuclear Power Plants. *Soil Dyn Earthq Eng* 2016;80:65–8.
- [9] Kausel E. Early history of soil–structure interaction. *Soil Dyn Earthq Eng* 2010;30(9):822–32.
- [10] Bhattacharya S, Nikitas G, Arany L, Nikitas N. Soil–structure interactions for offshore wind turbines. *IET Eng Technol Ref* 2017. <http://dx.doi.org/10.1049/etr.2016.0019>.
- [11] Katsanos EI, Thöns S, Georgakis CT. Wind turbines and seismic hazard: a state-of-the-art review. *Wind Energy* 2016;19(11):2113–33.
- [12] Hovind E, Kaynia AM. Earthquake response of wind turbine with non-linear soil-structure interaction. In *Proceedings of the 9th International Conference on Structural Dynamics, EURODYN*; 2014. p. 623–630.
- [13] Haciefendioğlu K. Stochastic seismic response analysis of offshore wind turbine including fluid-structure-soil interaction. *Struct Des Tall Spec Build* 2012;21(12):867–78.
- [14] Mardfekri M, Gardoni P. Probabilistic demand models and fragility estimates for offshore wind turbine support structures. *Eng Struct* 2013;52:478–87.
- [15] Kim DH, Lee SG, Lee IK. Seismic fragility analysis of 5 MW offshore wind turbine. *Renew Energy* 2014;65:250–6.
- [16] Kim DH, Lee GN, Lee Y, Lee IK. Dynamic reliability analysis of offshore wind turbine support structure under earthquake. *Wind Struct* 2015;21(6):609–23.
- [17] Zheng XY, Li H, Rong W, Li W. Joint earthquake and wave action on the monopile wind turbine foundation: an experimental study. *Mar Struct* 2015;44:125–41.
- [18] Alati N, Failla G, Arena F. Seismic analysis of offshore wind turbines on bottom-fixed support structures. *Philos Trans A* 2015;373(2035):20140086.
- [19] Chen J, Yang R, Ma R, Li J. Design optimization of wind turbine tower with lattice-tubular hybrid structure using particle swarm algorithm. *Struct Des Tall Spec Build* 2016;25(15):743–58.
- [20] Jonkman JM, Buhl Jr ML. FAST user's guide—updated august 2005 (No. NREL/TP-500-38230). Golden, CO: National Renewable Energy Laboratory (NREL); 2005.
- [21] Krathe VL, Kaynia AM. Implementation of a non-linear foundation model for soil-structure interaction analysis of offshore wind turbines in FAST. *Wind Energy* 2017;20(4):695–712.
- [22] Lombardi D, Bhattacharya S, Muir-Wood D. Dynamic soil–structure interaction of monopile supported wind turbines in cohesive soil. *Soil Dyn Earthq Eng* 2013;49:165–80.
- [23] Arany L, Bhattacharya S, Macdonald JH, Hogan SJ. Closed form solution of Eigen frequency of monopile supported offshore wind turbines in deeper waters incorporating stiffness of substructure and SSI. *Soil Dyn Earthq Eng* 2016;83:18–32.
- [24] Ptilakis K, Riga E, Anastasiadis A. Design spectra and amplification factors for Eurocode 8. *Bull Earthq Eng* 2012;10(5):1377–400.
- [25] Lotsberg I. Structural mechanics for design of grouted connections in monopile wind turbine structures. *Mar Struct* 2013;32:113–35.
- [26] Dallyn P, El-Hamalawi A, Palmeri A, Knight R. Experimental investigation on the development of wear in grouted connections for offshore wind turbine generators. *Eng Struct* 2016;113:89–102.
- [27] Patil A, Jung S, Kwon OS. Structural performance of a parked wind turbine tower subjected to strong ground motions. *Eng Struct* 2016;120:92–102.
- [28] CEN. Comité Europeen de Normalisation. Eurocode 3: design of steel structures, Part 1–1: general rules and rules for buildings. Comité Europeen de Normalisation, Brussels, Belgium; 2003.
- [29] McKenna F. OpenSees: a framework for earthquake engineering simulation. *Comput Sci Eng* 2011;13(4):58–66.
- [30] McGann CR, Arduino P, Mackenzie-Helnwein P. Applicability of conventional py relations to the analysis of piles in laterally spreading soil. *J Geotech Geoenviron Eng* 2011;137(6):557–67.
- [31] McGann CR, Arduino P, Mackenzie-Helnwein P. Simplified procedure to account for a weaker soil layer in lateral load analysis of single piles. *J Geotech Geoenviron Eng* 2012;138(9):1129–37.
- [32] Poulos HG. Pile behaviour—theory and application. *Geotechnique* 1989;39(3):365–415.
- [33] Dash S, Rouhoulamin M, Lombardi D, Bhattacharya S. A practical method for construction of p-y curves for liquefiable soils. *Soil Dyn Earthq Eng* 2017;97:478–81.
- [34] Carswell W, Arwade SR, DeGroot DJ, Lackner MA. Soil–structure reliability of offshore wind turbine monopile foundations. *Wind Energy* 2015;18(3):483–98.
- [35] API, American Petroleum Institute. Recommended practice for planning, designing and constructing fixed offshore platforms. API Recommended Practice 2A(RP-2A), Washington D.C, 17th edition; 1987.
- [36] Mosher RL. Load transfer criteria for numerical analysis of axial loaded piles in sand. Vicksburg: U.S. Army Engineering and Waterways Experimental Station, Automatic Data Processing Center; 1984.
- [37] Vijayvergiya, VN. Load-movement characteristics of piles. *Proc., Ports 77 Conf., ASCE, New York*; 1977.
- [38] Boulanger RW, Curras CJ, Kutter BL, Wilson DW, Abghari A. Seismic soil-pile-structure interaction experiments and analyses. *J Geotech Geoenviron Eng* 1999;125(9):750–9.
- [39] El Naggar MH, Shayanfar MA, Kimiaei M, Aghakouchak AA. Simplified BNWF model for nonlinear seismic response analysis of offshore piles with nonlinear input ground motion analysis. *Can Geotech J* 2005;42(2):365–80.
- [40] Wang S, Kutter BL, Chacko MJ, Wilson DW, Boulanger RW, Abghari A. Nonlinear seismic soil-pile structure interaction. *Earthq Spectra* 1998;14(2):377–96.
- [41] Shadlou M, Bhattacharya S. Dynamic stiffness of monopiles supporting offshore wind turbine generators. *Soil Dyn Earthq Eng* 2016;88:15–32.
- [42] Filippou FC, Popov EP, Bertero VV. Effects of bond deterioration on hysteretic behavior of reinforced concrete joints. Report EERC83-19, earthquake engineering research center. Berkeley: University of California; 1983.
- [43] Ballio G, Castiglioni CA. A unified approach for the design of steel structures under low and/or high cycle fatigue. *J Constr Steel Res* 1995;34(1):75–101.
- [44] Uriz P. Towards earthquake resistant design of concentrically braced steel structures [Doctoral Dissertation, Structural Engineering, Mechanics, and Materials]. Berkeley: Department of Civil and Environmental Engineering, University of California; 2005.
- [45] Dong RG. Effective mass and damping of submerged structures. Department of Energy. Report available at; 1978. http://www.iaea.org/inis/collection/NCLCollectionStore/_Public/09/411/9411273.pdf.
- [46] Yilmaz AS, Ozer Z. Pitch angle control in wind turbines above the rated wind speed by multi-layer perceptron and radial basis function neural networks. *Expert Syst Appl* 2009;36(6):9767–75.
- [47] ASCE, American Society of Civil Engineering. ASCE/SEI 07-10: Minimum Design Loads for Buildings and Other Structures. doi:10.1061/9780784412916; 2013.
- [48] Frohboese P, Schmuck C. Thrust coefficients used for estimation of wake effects for fatigue load calculation. In: *Proceedings of the European Wind Energy Conference, Warsaw, Poland*; 2010. p. 1–10.
- [49] Arany L, Bhattacharya S, Macdonald J, Hogan SJ. Design of monopiles for offshore wind turbines in 10 steps. *Soil Dyn Earthq Eng* 2017;92:126–52.
- [50] Avossa AM, Demartono C, Ricciardelli F. Assessment of the peak response of a 5MW HAWT under combined wind and seismic induced loads. *TOpen Constr Build Technol*. 2017;11:441–57.
- [51] Kjørlaus RA, Kaynia AM. Vertical earthquake response of megawatt-sized wind turbine with soil-structure interaction effects. *Earthq Eng Struct Dyn* 2015;44(13):2341–58.
- [52] Nikolaou S, Mylonakis G, Gazetas G, Tazoh T. Kinematic pile bending during earthquakes: analysis and field measurements. *Geotechnique* 2001;51(5):425–40.
- [53] Sica S, Mylonakis G, Simonelli AL. Transient kinematic pile bending in two-layer soil. *Soil Dyn Earthq Eng* 2011;31(7):891–905.
- [54] Di Laora R, Mandolini A, Mylonakis G. Insight on kinematic bending of flexible piles in layered soil. *Soil Dyn Earthq Eng* 2012;43:309–22.
- [55] Kuhn MJ. Dynamics and design optimization of offshore wind energy conversion systems. DUVIND Delft University Wind Energy Research Institute; 2001. [Report2001.002].
- [56] DNV, Det Norske Veritas. Guidelines for Design of Wind Turbines-DNV / Riso Code of Practice. USA; 2002.
- [57] Bisoi S, Haldar S. Dynamic analysis of offshore wind turbine in clay considering soil–monopile–tower interaction. *Soil Dyn Earthq Eng* 2014;63:19–35.
- [58] Chopra AK, McKenna F. Modeling viscous damping in nonlinear response history analysis of buildings for earthquake excitation. *Earthq Eng Struct Dyn* 2016;45(2):193–211.
- [59] CEN. Comité Europeen de Normalisation. Eurocode 3: Design of steel structures, Part 1-6: Strength and Stability of Shell Structures. Comité Europeen de Normalisation, Brussels, Belgium; 2007.
- [60] Gere JM, Goodno BJ. Mechanics of materials. 7th edn. Boston, MA: Cengage Learning; 2009. p. 1024.
- [61] Winterstetter TA, Schmidt H. Stability of circular cylindrical steel shells under combined loading. *Thin-Walled Struct* 2002;40(10):893–910.
- [62] Jalayer F, De Risi R, Manfredi G. Bayesian cloud analysis: efficient structural fragility assessment using linear regression. *Bull Earthq Eng* 2015;13(4):1183–203.
- [63] Foulser-Piggott R, Goda K. Ground motion prediction models for Arias intensity and cumulative absolute velocity for Japanese earthquakes considering single-station sigma and within-event spatial correlation. *Bull Seismol Soc Am* 2015;105(4):1903–18.
- [64] Boore DM. On pads and filters: processing strong-motion data. *Bull Seismol Soc Am* 2005;95(2):745–50.
- [65] Goda K, Wenzel F, De Risi R. Empirical assessment of non-linear seismic demand of mainshock–aftershock ground-motion sequences for Japanese earthquakes. *Front Built Environ* 2015;1:6.
- [66] Comité CEN. Comité Europeen de Normalisation Eurocode 8: Design of structures for earthquake resistance, Part 1: General rules, seismic actions and rules for buildings. Comité Europeen de Normalisation, Brussels, Belgium; 2004.
- [67] Kuramoto H. Seismic design codes for buildings in Japan. *J Disaster Res* 2006;1(3):341–56.
- [68] Vamvatsikos D, Cornell CA. Incremental dynamic analysis. *Earthq Eng Struct Dyn* 2002;31(3):491–514.
- [69] Lesgidis N, Sextos A, Kwon OS. Influence of frequency-dependent soil–structure interaction on the fragility of R/C bridges. *Earthq Eng Struct Dyn* 2017;46(1):139–58.
- [70] Baker JW. Quantitative classification of near-fault ground motions using wavelet analysis. *Bull Seismol Soc Am* 2007;97(5):1486–501.